Deposition path planning-integrated structural topology optimization for 3D additive manufacturing subject to self-support constraint

Jikai Liu[a,b], Albert C. To[b*]

[a]Department of Mechanical Engineering, University of Alberta, Edmonton, Canada

[b]Department of Mechanical Engineering and Materials Science, University of Pittsburgh, Pittsburgh, Pennsylvania 15261, USA

*Corresponding author. Email: albertto@pitt.edu

Abstract

This paper presents a novel level set-based topology optimization implementation, which addresses two main problems of design-for-additive manufacturing (AM): the material anisotropy and the self-support manufacturability constraint. AM material anisotropy is widely recognized and taking it into account while performing structural topology optimization could more realistically evaluate the structural performance. Therefore, both build direction and in-plane raster directions are considered by the topology optimization algorithm, especially for the latter, which are calculated through deposition path planning. The self-support manufacturability constraint is addressed through a novel multi-level set modeling. The related optimization problem formulation and solution process are demonstrated in details. It is proved by several numerical examples that, the manufacturability constraints are always strictly satisfied. Marginally, the recently popular structural skeleton-based deposition paths are also employed to assist the structural topology optimization, and its characteristics are discussed.

Keywords: Deposition path planning; Topology optimization; Additive manufacturing; Manufacturability constraint

1. Introduction

Additive manufacturing (AM), also known as 3D printing, refers to a series of processes which produce the part through the layer-by-layer material deposition. It has demonstrated the outstanding characteristic that, the part can be in any geometric complexity and many manufacturability constraints of the traditional subtractive machining are eliminated. Hence, AM is greatly preferred by the design community for the extremely enhanced degrees of design freedom.

Therefore, design methodology for AM parts has attracted plenty of attentions. Strategically, several design for AM (DfAM) frameworks have been proposed. Rosen [1] proposed the process-structure-property-behavior framework for cellular structures, where the idea of manufacturing planning-assisted structural performance evaluation was proposed. Ponche [2] proposed a global DfAM framework where the build direction, the part geometry and the deposition paths are consecutively designed. However, a drawback of the consecutive process is the reduced design optimality, especially compared to the concurrent design process. Part consolidation is also an active DfAM research direction, where the

function surface and function volume concepts have been widely explored to realize the function integration [3,4]. Liu [5] evaluated the structural performance of consolidated AM parts through topology optimization and accordingly, proposed the guidelines for part consolidation.

More specifically, topology optimization has been widely adopted as the main methodology for embodiment design of AM parts [6], because it performs the freeform shape and topology evolution, and thus, produces very complex geometry which fits the characteristic of AM. Several aspects have been actively investigated about the topology optimization for AM, such as the lattice structure design [7–9], the multi-material structure design [10,11], the support-free manufacturability constraint [12–14], the minimum component size issue [15,16], and the design interpretation [17,18], etc. Even so, as summarized in [15,19,20], a lack of feasible solutions is still the situation for many AM-related problems.

In this work, we intend to address the AM-induced material anisotropy when dealing with the topology optimization problem, and at the same time, solve the self-support manufacturability constraint.

Material anisotropy is a phenomenon caused by the layer-by-layer deposition process, where the material properties could be very different along the build direction, the in-layer raster direction, and the in-layer transverse direction. This phenomenon is widely recognized and extensive experimental studies have been conducted for disclosure [21–25]. The general conclusion is that, the material properties are stronger in the in-layer raster direction, and those in the build direction are the weakest, especially for polymer printing. Moreover, these experimental results have been embedded into finite element programs to improve the numerical analysis accuracy [26–28], and some [27,29] have utilized the experimental data to optimize the build direction to enhance the structural performance.

On the other hand, there exists the gap that, the AM induced material anisotropy is rarely addressed by topology optimization implementations, with the exception, Liu [5] performed the concurrent build direction and structural topology optimization for 2D cases. However, 3D study would be practically more meaningful, even though the problem complexity is drastically increased. Especially within each printing layer, the material properties depend on the planned deposition paths, and the design problem is transformed into a concurrent multi-layer deposition path planning and structural topology optimization problem. Recently, Smith and Hoglund [30] explored the raster direction optimization and realized the optimized printing paths into real parts. However, a limitation is that, the raster directions are treated as discrete orientation variables but the continuity could be low. Liu and Yu [31] performed the concurrent raster direction and topology optimization by building the continuous contour-offset printing paths and additionally, addressed the optimal printing path design for fixed geometry problems through the radial basis function (RBF) fitting and level set modeling. These two works targeted the planar problems, but to the best of the authors' knowledge, there is no extension to 3D. Innovatively, we contribute a multi-level set-based method to solve the 3D concurrent design problems. Multiple level set functions are employed to represent the sliced printing layers and facilitate the related deposition path planning. It is worth noticing that, the build direction is assumed to be fixed for the sake of simplicity.

Level set method is a well-established structural topology optimization method. Osher and Sethian [32] initially proposed the level set to be an interface modeling and propagating method, and later, Wang et al. [33] and Allaire et al. [34] developed the structural topology optimization method under the level set framework. It has several advantages compared to other topology optimization methods, such as the clear-cut interface representation, the always available interface-related information (e.g. curvature), and the

parameterized [35] and feature-based [36,37] geometry representation, etc. In the past decade, extensive research efforts have been spent on level set topology optimization [38] subject to diversified physical disciplines, e.g. solid mechanics [33,34], fluid dynamics [39], and thermal dynamics [40,41] etc. Another reason for employing the level set method is that, it has been used for tool path planning for traditional contour machining, which derives the contour-offset tool paths based on the signed distance information [42,43]. Hence, it is feasible to perform the deposition path planning-integrated structural topology optimization under the unified level set framework. Other than the contour-offset path pattern, a novel structural skeleton-based path pattern is realized under the level set framework, which is a highlight of this paper. Skeleton is a lower dimensional description of the object. As defined by Blum [44], it is the locus of all the interior maximal circles for 2D or spheres for 3D, and thus, the skeleton points together with the related interior maximal circles/spheres form a complete description of the geometry. In recent years, the skeleton concept has been used in topology optimization field to measure and control the component length scale, under both density-based [45] and level set [46,47] frameworks, because the interior maximal circles/spheres can effectively measure the local component length scale. In addition, the structural skeleton has also been used to generate deposition paths for additive manufacturing [48,49].

Another contribution of this work is that, the self-support manufacturability constraint issue is addressed for 3D structures. This manufacturability constraint arises at surface regions whose angle of inclination is smaller than the threshold value, which are also known as overhangs. Supports are required to prevent these overhangs from distortion or even collapse. However, utilization of the support requires additional design and pre-processing effort, wastes material, and lengthens the printing process. Therefore, self-support topology optimization has been actively investigated. Hu et al. [50] slimmed the support through a shape optimization approach. Mirzendehdel and Suresh [51] transformed the part design into a multi-objective topology optimization problem with a balanced objective function between the support material consumption and structural compliance. Bracket et al. [15] proposed a solution to repeatedly linearize the boundary segments and accordingly, penalize the unbuildable ones; however, this solution remains to be a conceptual idea. Leary et al. [12] proposed a post-treatment method to add materials to the overhang areas. This method has been proven effective, but the result optimality is sacrificed. Gaynor [13,52] realized the overhang-free control through an additional layer of design variable projection. Langelaar [14,53] proposed another type of density filter which achieved similar overhang free design effects. A limitation of the density filter-based method is that, the extra-layer of density filter greatly increases the sensitivity-related computational cost [14,52]. Very recently, Qian [54] developed a Heaviside projection based integration function to penalize the undercut or overhang areas. Wu et al. [55] explored the self-support issue of porous infill by using the rhombic cells. In summary, existing methods have partially addressed the self-support manufacturability constraint but it still deserves more exploration for better computational efficiency and robustness. Therefore, a multi-level set-based method is contributed in this work to address this self-support manufacturability issue, about which more details will be specified in the later sections.

It is noted that, this paper contributes to two topics: the deposition path-integrated design and the self-support design. For the former, it is useful for the fused deposition modeling (FDM) process; while for the latter, it employs the general applicability for support-required AM processes.

2. Level set method

Generally, the level set function $\Phi(x,y)$: $R^n \longmapsto R$, describes the geometry as presented in Eq. (1).

$$\begin{cases} \Phi(x,y) > 0, & x,y \in \Omega/\partial\Omega \\ \Phi(x,y) = 0, & x,y \in \partial\Omega \\ \Phi(x,y) < 0, & x,y \in D/\Omega \end{cases} \tag{1}$$

where Ω represents the material domain, D indicates the entire design domain, and thus D/Ω represents the void.

It provides an implicit approach for geometry description and accordingly, performing the contour-offset deposition path planning was previously studied and the method is inherited in this work. Moreover, we propose a novel approach to addressing the self-support constraint based on the multi-level set interpolation technique. The numerical details will be presented at the rest of this section.

2.1 Contour-offset path planning through level set

Under the discrete level set framework, level set values are defined on the finite element mesh nodes and Eq. (2) is usually solved to initialize the level set field to follow the signed distance convention. Therefore, level set is effective in offsetting the structural boundary by easily extracting the iso-value level set contours. This technique was previously applied to generate the tool paths for the traditional contour machining [42,43], which can be trivially extended to plan the deposition paths for AM; see Fig. 1 for two examples.

$$|\nabla\Phi(x,y)| = 1 \tag{2}$$

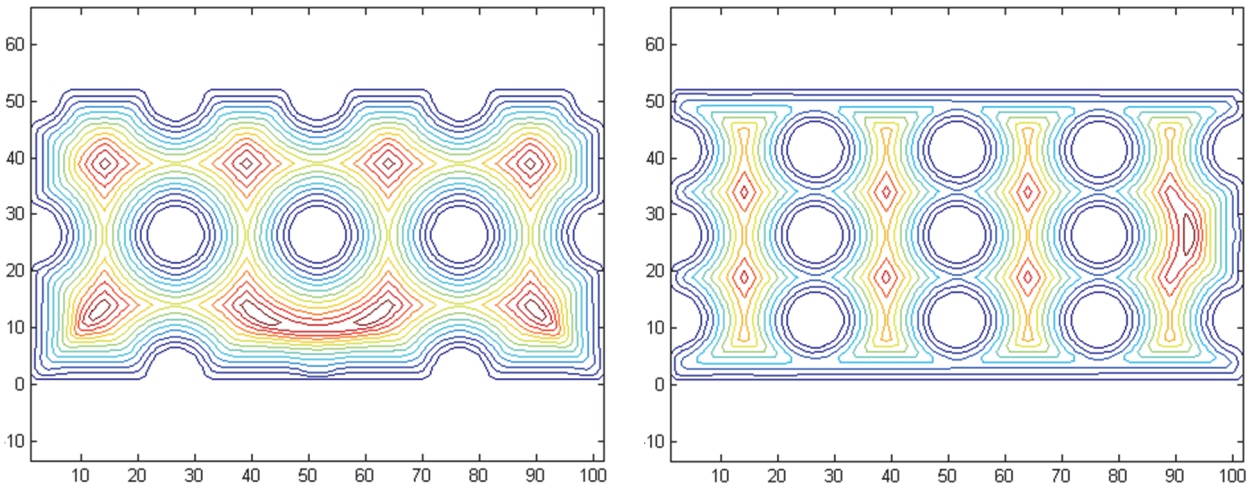

Fig. 1 Two examples of the level set-based deposition paths of the contour-offset pattern

Given the technical merits, the level set method can effectively and efficiently generate the deposition paths, regardless of the geometric complexity.

Then, the local deposition orientation can be analytically expressed by Eq. (3) [56].

$$\theta = \frac{\pi}{2} + \arctan\left(\frac{\partial \Phi / \partial y}{\partial \Phi / \partial x}\right) \tag{3}$$

According to the classic laminate theory, the elasticity tensor including the in-layer orientation variable θ is expressed by Eq. (4).

$$\boldsymbol{D}(\theta) = \boldsymbol{K}(\theta)\boldsymbol{D}^0\boldsymbol{K}(\theta)^T \tag{4}$$

where $\boldsymbol{D}$ is the elasticity tensor given the in-layer deposition orientation θ, and $\boldsymbol{D}^0$ is the elasticity tensor when θ equals to zero. $\boldsymbol{K}(\theta)$ stands for the coordinate transformation tensor. The orientation variable θ is defined in Fig. 2.

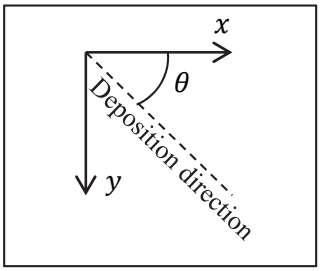

Fig. 2 Definition of the orientation variable

2.2 Multi-level set modeling of AM parts

Multi-level set modeling has been widely applied to diversified multi-material topology optimization problems, such as the 'color' level set [57–60] and the MMLS (Multi-Material Level Set) [61]. But in fact, multi-level set modeling can have broader applicability, especially for those which involve only a single material type but still require interpolation of multiple level set functions, e.g. the product family design as conducted in [62].

Innovatively in this work, multiple level set functions are employed to represent the sliced homogeneous AM part, and a novel interpolation of the multiple level set functions is proposed to address the self-support manufacturability constraint.

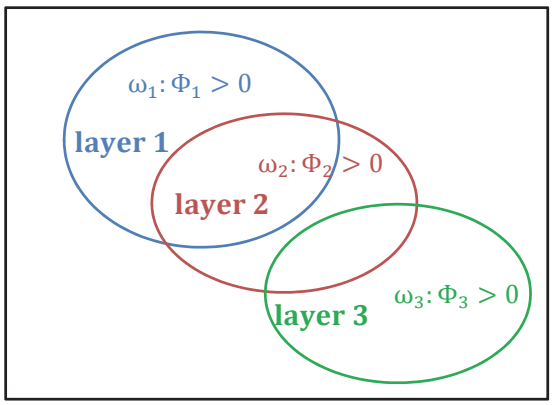

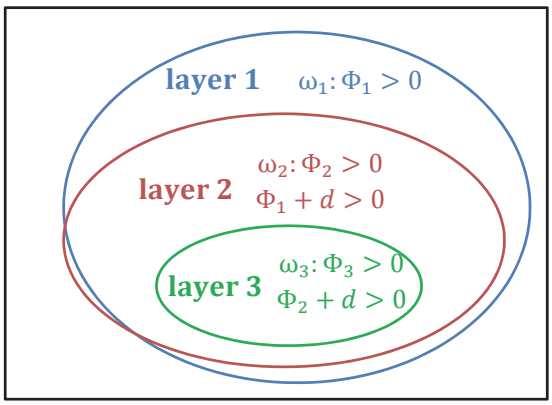

(a) Multi-layer modeling

(b) Multi-layer modeling subject to the manufacturability constraint

Fig. 3 Multi-level set based modeling

To be specific, figure 3a presents an example of the multi-level set modeling. There are three printing layers, each of which is represented by an independent level set function. Therefore, each layer is expressed by Eq. (5).

$$\omega_i = \{x, y \,|\Phi_i(x, y) > 0\} \tag{5}$$

For a step forward, if the self-support manufacturability constraint is considered, the layers cannot be independently defined and the material domain of a higher layer should be constrained with a maximum overhang distance of d. Therefore, a modified representation of the layers is presented in Eq. (6); also see Fig. 3b.

$$\begin{aligned} \omega_1 &= \{(x, y) \,|\Phi_1(x, y) > 0\} \\ \omega_i &= \{(x, y) \,|\Phi_i(x, y) > 0, \Phi_{i-1}(x, y) + d > 0\}, \;\; i > 1 \end{aligned} \tag{6}$$

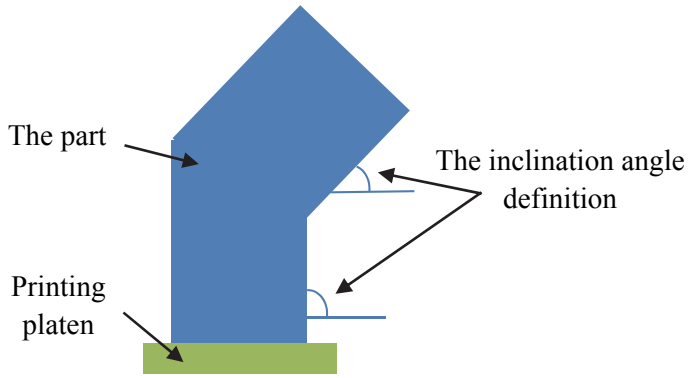

Fig. 4 The inclination angle definition

Specifically about the d, it is calculated through Eq. (7), based on the layer height h and the threshold inclination angle γ for self-support. Definition of the inclination angle is shown in Fig. 4.

$$d = h/\tan(\gamma) \tag{7}$$

(a) $d \neq 0$ and $\gamma = 45°$

(b) $d = 0$

Fig. 5. Design space comparison from a 2D view

In practice, h tends to be small and γ varies within the range of $[30°, 60°]$ depending on the specific AM process. Therefore, d tends to be a small positive value and in case that only a limited number of printing layers are involved, assuming $d = 0$ would not have a major impact on the design space size; refer to Figure 5 for an example. Hence, according to the geometric characteristics of the part, we distinguish the optimization problem into two types with different levels of solving complexity: (i) if the overall printing height is much smaller in length scale compared to the other two dimensions, d can be assumed to be zero which will greatly simplify the later sensitivity analysis, as demonstrated in Section 4; (ii) otherwise, d cannot be ignored and the regular adjoint sensitivity result has to be post-processed; see the details in Section 5.

By assuming $d = 0$ of problem type 1, the material interpolation is realized through Eq. (8).

$$\boldsymbol{D}_i(x,y) = \prod_{j=1}^{i} H\left(\Phi_j(x,y)\right) \boldsymbol{D}(\theta(\Phi_i)) \tag{8}$$

where H means the Heaviside function and, i and j are the layer index.

Otherwise, the problem type 2 with the material interpolation as shown Eq. (9) will be explored.

$$\begin{gathered} \boldsymbol{D}_i(x,y) = H\big(\Phi_{\mathrm{i}}(x,y)\big)H(\Phi_{i-1}(x,y) + d)\boldsymbol{D}(\theta(\Phi_i)), \qquad i > 1 \\ \boldsymbol{D}_1(x,y) = H\big(\Phi_1(x,y)\big)\boldsymbol{D}(\theta(\Phi_i)) \end{gathered} \tag{9}$$

3. Optimization problem type 1

3.1 Problem formulation and solution

Subject to Eq. (8), the conventional compliance minimization problem is formulated as shown below:

$$\begin{gathered} \text{min.} \quad J = \sum_{i=1}^{N} \left[\int_D \boldsymbol{D}(\theta(\Phi_i))\boldsymbol{e}(\boldsymbol{u}_i)\boldsymbol{e}(\boldsymbol{u}_i) \prod_{j=1}^{i} H\left(\Phi_j(x,y)\right) d\Omega_i \right] \\ s.t. \quad a(\boldsymbol{u},\boldsymbol{v},\boldsymbol{\Phi}) = l(\boldsymbol{v}), \qquad \forall \boldsymbol{v} \in U_{ad} \\ V = \sum_{i=1}^{N} \int_D H(\Phi_i) d\Omega_i \le V_{max} \\ a(\boldsymbol{u},\boldsymbol{v},\boldsymbol{\Phi}) = \sum_{i=1}^{N} \left[\int_D \boldsymbol{D}\big(\theta(\Phi_i)\big)\boldsymbol{e}(\boldsymbol{u}_i)\boldsymbol{e}(\boldsymbol{v}_i) \prod_{j=1}^{i} H\left(\Phi_j(x,y)\right) d\Omega_i \right] \\ l(\boldsymbol{v}) = \int_{\partial\Omega} \boldsymbol{\tau} \cdot \boldsymbol{v} d\Gamma \end{gathered} \tag{10}$$

in which $a(\ \ )$ is the energy bilinear form and $l(\ \ )$ is the load linear form. The load linear expression does not include $\boldsymbol{\Phi}$, because it is assumed that the area applied of boundary traction force $\boldsymbol{\tau}$ is non-designable. $\boldsymbol{u}_i$and $\boldsymbol{v}_i$ are the deformation vector and the test vector within the i^{th} printing layer, and $\boldsymbol{e}(\ \ )$ is the strain. $U_{ad} = \{\boldsymbol{v} \in H^1(\Omega)^d | \boldsymbol{v} = 0 \ on \ \Gamma_D\}$ is the space of kinematically admissible displacement field. The body forces are ignored in this work.

Material derivative and the adjoint method are employed to perform the shape sensitivity analysis.

To be specific, the Lagrangian is constructed in Eq. (11).

$$L = J + a(\boldsymbol{u}, \boldsymbol{w}, \boldsymbol{\Phi}) - l(\boldsymbol{w}) + \lambda(\sum_{i=1}^{N} \int_D H(\Phi_i) d\Omega_i - V_{max}) \tag{11}$$

Then, material derivative of the Lagrangian is presented in Eq. (12).

$$L' = J' + a'(\boldsymbol{u}, \boldsymbol{w}, \boldsymbol{\Phi}) - l'(\boldsymbol{w}) + \lambda(\sum_{i=1}^{N} \int_D H(\Phi_i) d\Omega_i - V_{max})' \tag{12}$$

where,

$$\begin{aligned} J' = {} & 2\sum_{i=1}^{N}\left[\int_D \boldsymbol{D}\big(\theta(\Phi_i)\big)\boldsymbol{e}(\boldsymbol{u}_i')\boldsymbol{e}(\boldsymbol{u}_i)\prod_{j=1}^{i} H\left(\Phi_j(x,y)\right) d\Omega_i\right] \\ & + \sum_{i=1}^{N}\left[\sum_{k=1}^{i}\int_D \boldsymbol{D}\big(\theta(\Phi_i)\big)\boldsymbol{e}(\boldsymbol{u}_i)\boldsymbol{e}(\boldsymbol{u}_i)\delta\big(\Phi_k(x,y)\big)\prod_{j=1,j\neq k}^{i} H\left(\Phi_j(x,y)\right) V_{nk}|\nabla\Phi_k| d\Omega_i\right] \end{aligned} \tag{13}$$

$$\begin{aligned} a'(\boldsymbol{u}, \boldsymbol{w}, \boldsymbol{\Phi}) = {} & \sum_{i=1}^{N}\left[\int_D \boldsymbol{D}\big(\theta(\Phi_i)\big)\boldsymbol{e}(\boldsymbol{u}_i')\boldsymbol{e}(\boldsymbol{w}_i)\prod_{j=1}^{i} H\left(\Phi_j(x,y)\right) d\Omega_i\right] \\ & + \sum_{i=1}^{N}\left[\int_D \boldsymbol{D}\big(\theta(\Phi_i)\big)\boldsymbol{e}(\boldsymbol{u}_i)\boldsymbol{e}(\boldsymbol{w}_i')\prod_{j=1}^{i} H\left(\Phi_j(x,y)\right) d\Omega_i\right] \\ & + \sum_{i=1}^{N}\left[\sum_{k=1}^{i}\int_D \boldsymbol{D}\big(\theta(\Phi_i)\big)\boldsymbol{e}(\boldsymbol{u}_i)\boldsymbol{e}(\boldsymbol{w}_i)\delta\big(\Phi_k(x,y)\big)\prod_{j=1,j\neq k}^{i} H\left(\Phi_j(x,y)\right) V_{nk}|\nabla\Phi_k| d\Omega_i\right] \end{aligned} \tag{14}$$

$$l'(\boldsymbol{v}) = \int_{\partial\Omega} \boldsymbol{\tau} \cdot \boldsymbol{w}' d\Gamma \tag{15}$$

$$\left(\sum_{i=1}^{N}\int_D H(\Phi_i) d\Omega_i - V_{max}\right)' = \sum_{i=1}^{N}\int_D \delta\big(\Phi_i(x,y)\big) V_{ni}|\nabla\Phi_i| d\Omega_i \tag{16}$$

Substitute Eq. (13-16) into Eq. (12). Collect all the terms including $\boldsymbol{w}$ and the sum is naturally equivalent to zero; see Eq. (17).

$$\sum_{i=1}^{N}\left[\int_{D}\boldsymbol{D}\big(\theta(\Phi_i)\big)\boldsymbol{e}(\boldsymbol{u}_i)\boldsymbol{e}(\boldsymbol{w}_i{}')\prod_{j=1}^{i}H\left(\Phi_j(x,y)\right)d\Omega_i\right]-\int_{\partial\Omega}\boldsymbol{\tau}\cdot\boldsymbol{w}'d\Gamma=0 \tag{17}$$

Then, collect the terms including $\boldsymbol{u}'$ and force the sum equivalent to zero, which is:

$$\begin{aligned}&2\sum_{i=1}^{N}\left[\int_{D}\boldsymbol{D}\big(\theta(\Phi_i)\big)\boldsymbol{e}(\boldsymbol{u}_i{}')\boldsymbol{e}(\boldsymbol{u}_i)\prod_{j=1}^{i}H\left(\Phi_j(x,y)\right)d\Omega_i\right]\\&+\sum_{i=1}^{N}\left[\int_{D}\boldsymbol{D}\big(\theta(\Phi_i)\big)\boldsymbol{e}(\boldsymbol{u}_i{}')\boldsymbol{e}(\boldsymbol{w}_i)\prod_{j=1}^{i}H\left(\Phi_j(x,y)\right)d\Omega_i\right]=0\end{aligned} \tag{18}$$

By solving Eq. (18), solution of the adjoint variable $\boldsymbol{w}=-\boldsymbol{2u}$ is derived. Then, by collecting the remaining terms, the sensitivity result is obtained as:

$$\begin{aligned}L'=-\sum_{i=1}^{N}\left[\sum_{k=1}^{i}\int_{D}\boldsymbol{D}\big(\theta(\Phi_i)\big)\boldsymbol{e}(\boldsymbol{u}_i)\boldsymbol{e}(\boldsymbol{u}_i)\delta\big(\Phi_k(x,y)\big)\prod_{j=1,j\neq k}^{i}H\left(\Phi_j(x,y)\right)V_{nk}|\nabla\Phi_k|d\Omega_i\right]\\+\lambda\sum_{i=1}^{N}\int_{D}\delta\big(\Phi_i(x,y)\big)V_{ni}|\nabla\Phi_i|d\Omega_i\end{aligned} \tag{19}$$

Therefore,

$$V_{nk}=-\lambda+\sum_{i=k}^{N}\left[\boldsymbol{D}\big(\theta(\Phi_i)\big)\boldsymbol{e}(\boldsymbol{u}_i)\boldsymbol{e}(\boldsymbol{u}_i)\prod_{j=1,j\neq k}^{i}H\left(\Phi_j(x,y)\right)\right] \tag{20}$$

which guarantees that $L'\leq 0$.

3.2 Numerical examples

For all the numerical examples, the finite element analysis is performed based on fixed hexahedral meshes and the artificial weak material properties are adopted by the voids in order to prevent the singularity problem; see Eq. (21).

$$\boldsymbol{D}_v=10^{-3}\boldsymbol{D} \tag{21}$$

in which $\boldsymbol{D}_v$ is the elasticity tensor of the void.

The volume constraint is addressed through the Augmented Lagrange method which has the Lagrange multiplier as:

$$\begin{aligned}\lambda_{k+1}&=\lambda_k+\mu_k\Big(\sum_{i=1}^{N}\int_{D}H(\Phi_i)d\Omega_i-V_{max}\Big)\\\mu_{k+1}&=\beta\mu_k\ \ where\ 0<\beta<1\end{aligned} \tag{22}$$

in which μ is the penalization factor and β is its adjustment parameter.

The material properties tested by [27] are employed for the numerical examples, as specified in Table 1. The orthotropic elastic model is assumed.

Table 1 3D printing material properties

Directions	Young's modulus (GPa)	Shear modulus (GPa)	Poisson's ratio
In-plain raster direction	1.16	0.51	0.09
In-plain transverse direction	1.05	0.28	0.37
Build direction	0.52	0.30	0.31

3.2.1 Case 1

Boundary conditions (BCs) of the first case are demonstrated in Fig. 6, where the dark blue-colored elements are fixed and, the in-plane and out-of-plane point forces of the magnitude 100kN are separately applied. The design domain is of size 40cm*20cm*4cm, where four printing layers exist. The objective is to minimize the structural compliance under the maximum material volume ratio of 0.4. The starting topology for all the layers is shown in Fig. 6c. This starting topology is inherited by all the numerical examples in Section 3 and 4, unless otherwise noted.

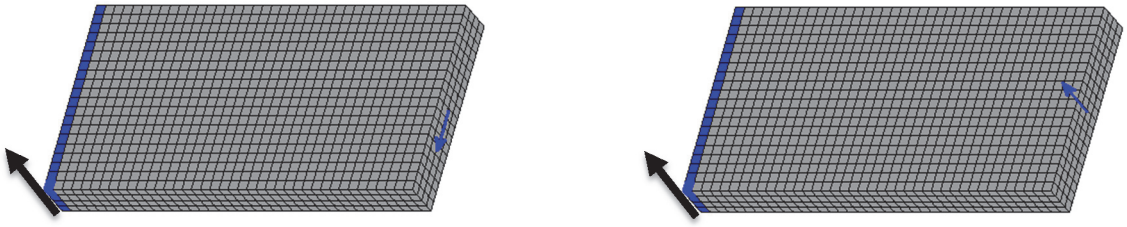

(a) BC 1 (b) BC 2

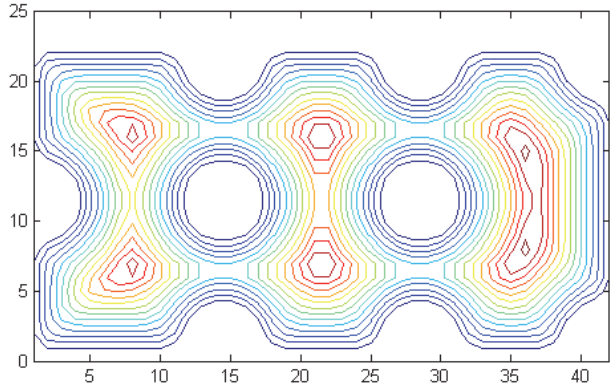

(c) Starting topology of all the layers

Fig. 6 Boundary conditions of case 1 (the build direction is specified by the bolded arrow)

Correspondingly, the optimization results are layer-wisely demonstrated in Fig. 7 and Fig. 8, respectively, where a smaller index means a lower-level printing layer.

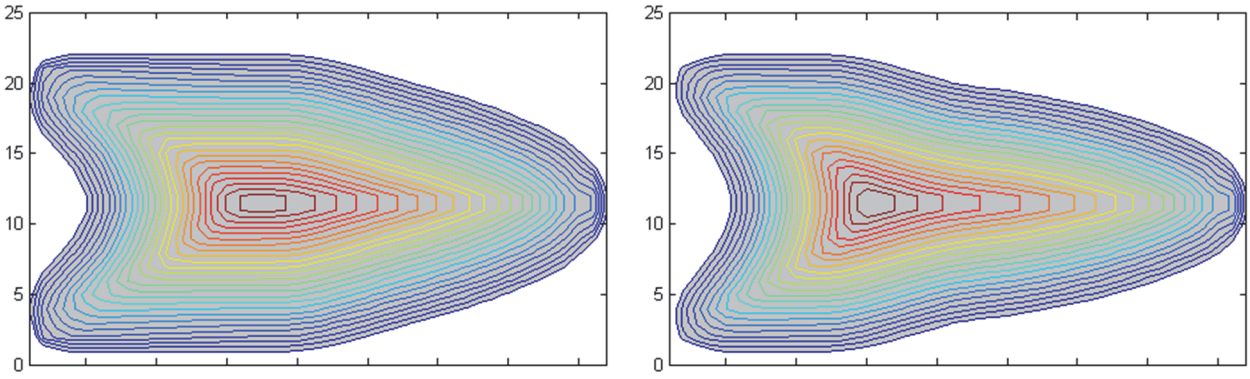

(a) Layer 1 (b) Layer 2

Fig. 7 Layer-wise optimization results of BC1 (Compliance = 24.89kN·m)

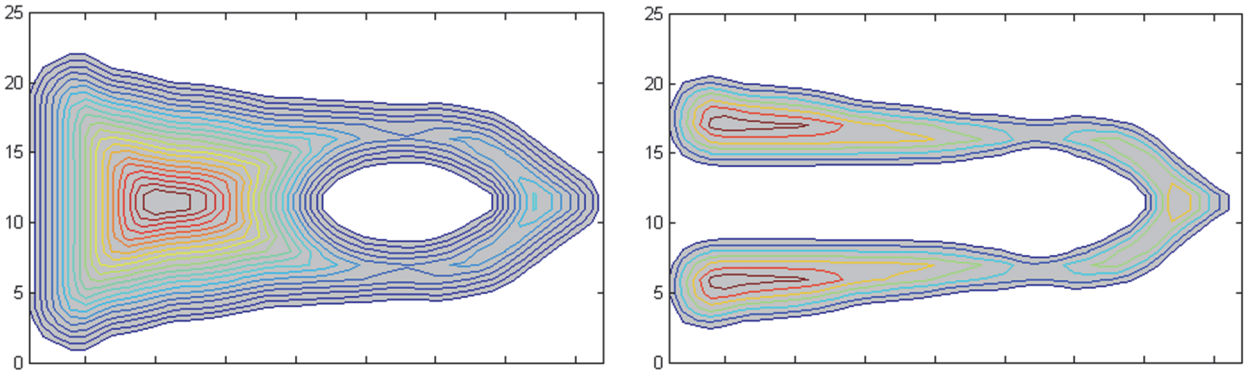

(a) Layer 1 (b) Layer 2

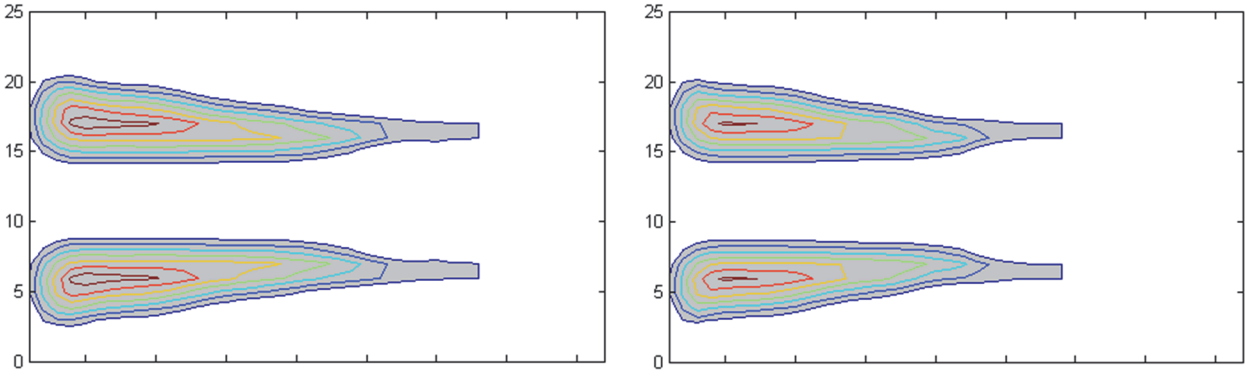

(c) Layer 3 (d) Layer 4

Fig. 8 Layer-wise optimization results of BC2 (Compliance = 421.60kN·m)

A few conclusions can be drawn from the optimization results that:

(i) In the optimization results of BC 1, layer 3 and layer 4 totally disappear while only the first two layers remain. In addition, the support-free manufacturability constraints are strictly satisfied.

(ii) In the optimization results of BC 2, all the layers remain and at the same time, the support-free manufacturability constraints are strictly satisfied. In layer 3 and layer 4, foot ribs are generated to bear the bending load, which is reasonable.

The convergence histories are demonstrated in Fig. 9.

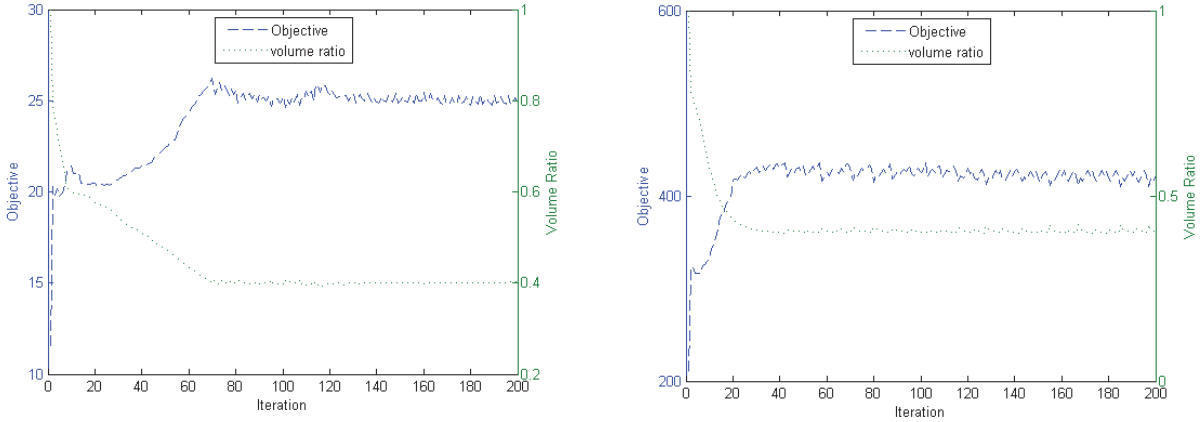

(a) BC1 (b) BC 2

Fig. 9 Convergence histories (the y-axis has the unit of kN·m)

For BC1, if we modify the starting topology by changing the interior hole distribution; see Fig. 10a, the topology optimization result is updated as presented in Fig. 10(b-c), where the result is slightly different as compared to Fig. 7: (i) the layer 3 is not totally removed, and (ii) the structural compliance is slightly smaller but no significant improvement has been observed. Therefore, for this example, the optimization result is but not strongly dependent on the starting topology.

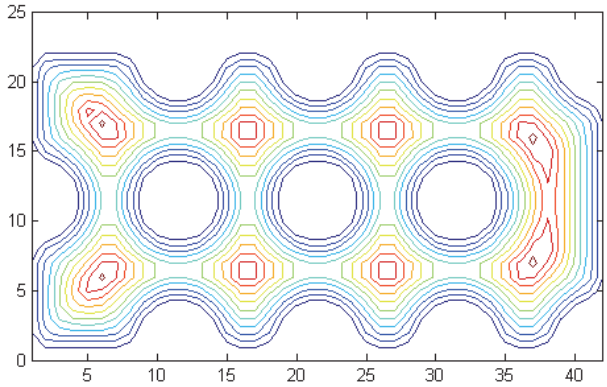

(a) Modified starting topology of all the layers

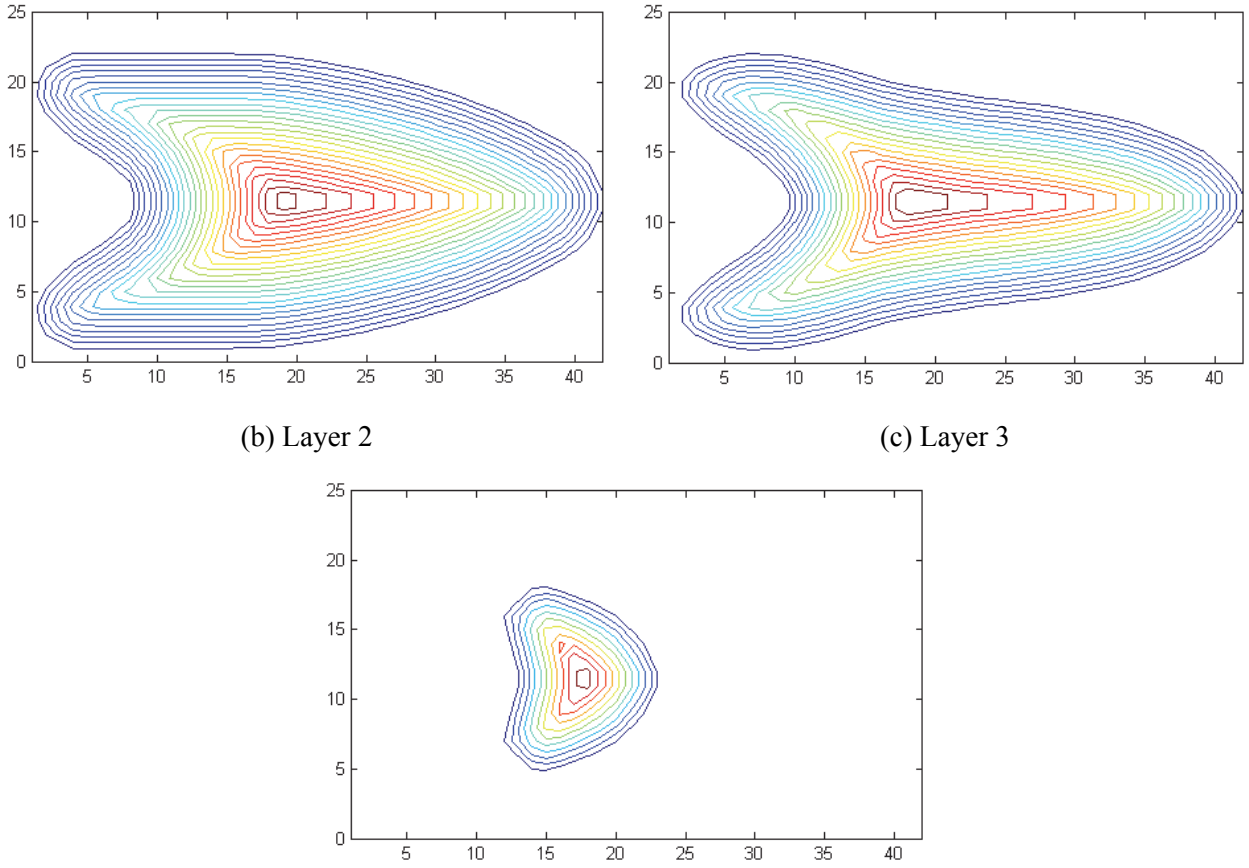

(b) Layer 2 (c) Layer 3

(d) Layer 4

Fig. 10 Layer-wise optimization results of BC1 by modifying the starting topology (Compliance = 24.07kN·m)

Other than that, the design result of BC1 without considering the self-support requirement is demonstrated in Fig. 11. We can see that, the derived structural compliance is reduced by 8.47 percent as compared to the result shown in Fig. 7; however, a support volume fraction of 8.37 percent is required, which means 20.92 percent of materials consumed by the part. Therefore, whether or not considering the self-support requirement depends on the specific need of less material consumption or better structural performance.

In addition, by comparing the results as shown in Fig. 7 and 11, the material distribution in layer 1 of the former is drastically increased because of the self-support constraint. Therefore, to balance the overall material consumption, the materials in layer 3 and 4 in Fig. 7 disappear.

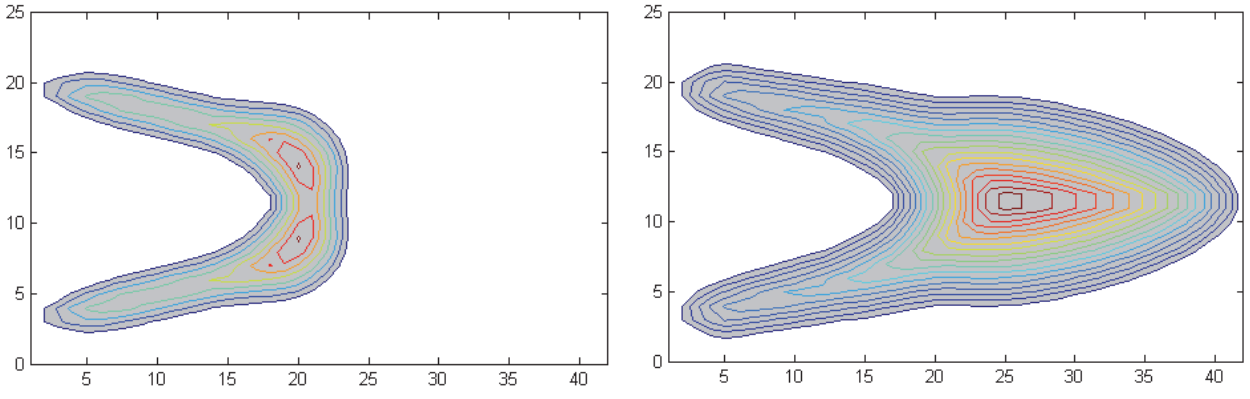

(a) Layer 1 (b) Layer 2

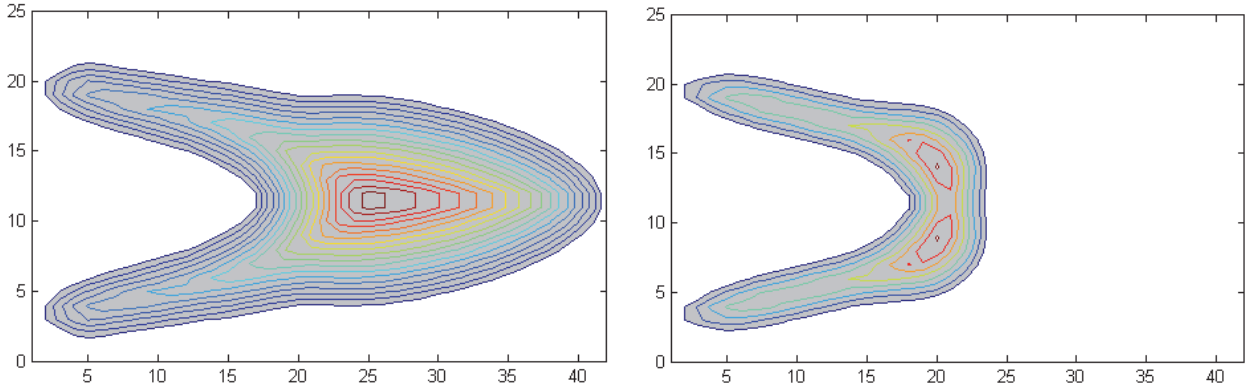

(c) Layer 3 (d) Layer 4

Fig. 11 Layer-wise optimization results of BC1 without considering self-support requirement (Compliance = 22.78kN·m)

3.2.2 Case 2

Boundary conditions (BCs) of the second case studied are demonstrated in Fig. 12, where the dark blue-colored elements are fixed and the in-plane and out-of-plane point forces of the magnitude 100kN are separately applied. The design domain is of size 40cm*20cm*4cm, where four printing layers exist. The objective is to minimize the structural compliance under the maximum material volume ratio of 0.4.

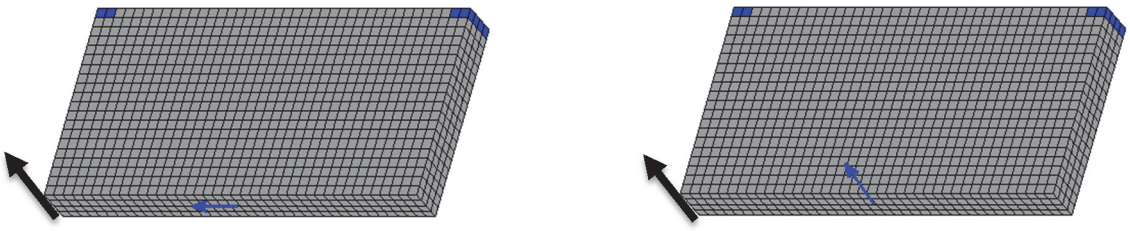

(a) BC 1 (b) BC 2

Fig. 12 Boundary conditions of case 2 (the build direction is specified by the bolded arrow)

Correspondingly, the optimization results are layer-wisely demonstrated in Fig. 13 and Fig. 14, respectively, where a smaller index means a lower-level layer.

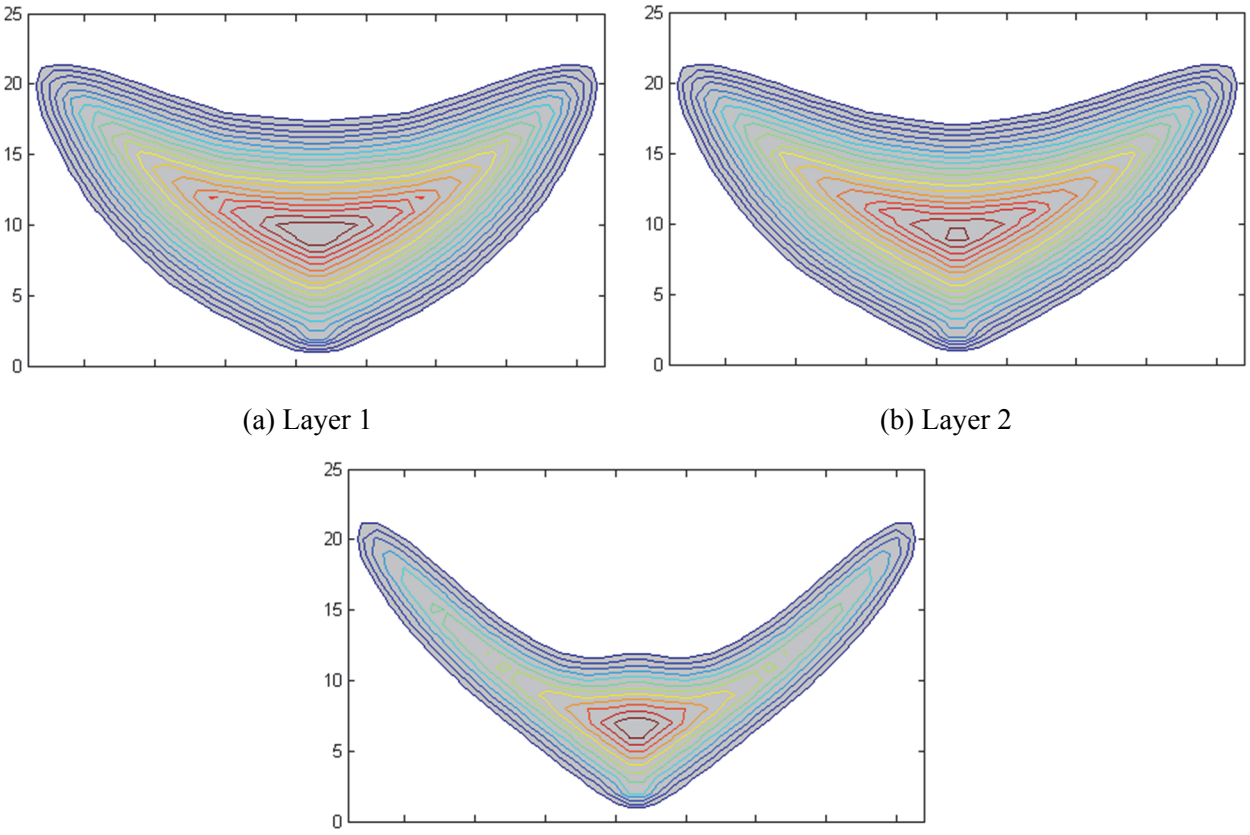

(a) Layer 1 (b) Layer 2

(c) Layer 3

Fig. 13 Layer-wise optimization results of BC1 (Compliance = 4.07kN·m)

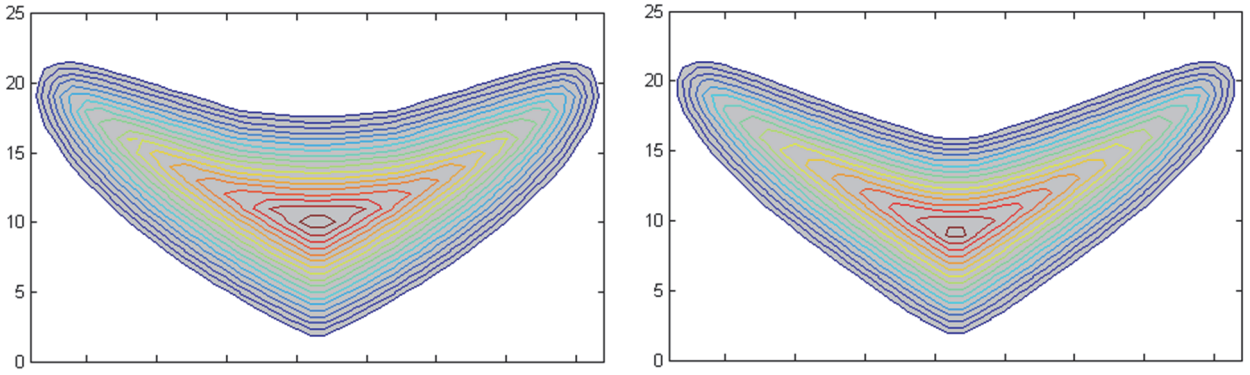

(a) Layer 1 (b) Layer 2

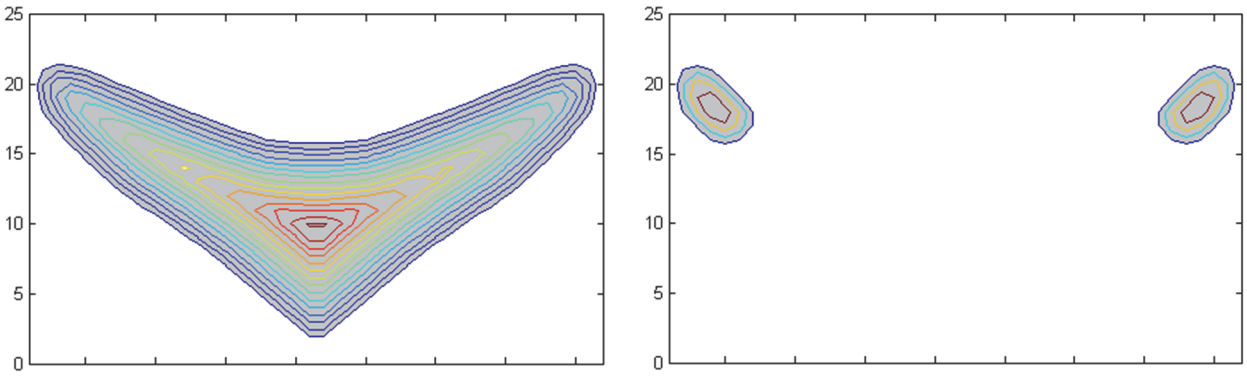

(c) Layer 3 (d) Layer 4

Fig. 14 Layer-wise optimization results of BC2 (Compliance = 204.19kN·m)

A few conclusions can be drawn from the optimization results that:

(i) In the optimization results of BC 1, the layer 4 totally eliminates while the other three layers remain. In addition, the support-free manufacturability constraints are strictly satisfied.

(ii) In the optimization results of BC 2, all the layers remain and at the same time, the support-free manufacturability constraints are strictly satisfied.

Convergence histories are demonstrated in Fig. 15.

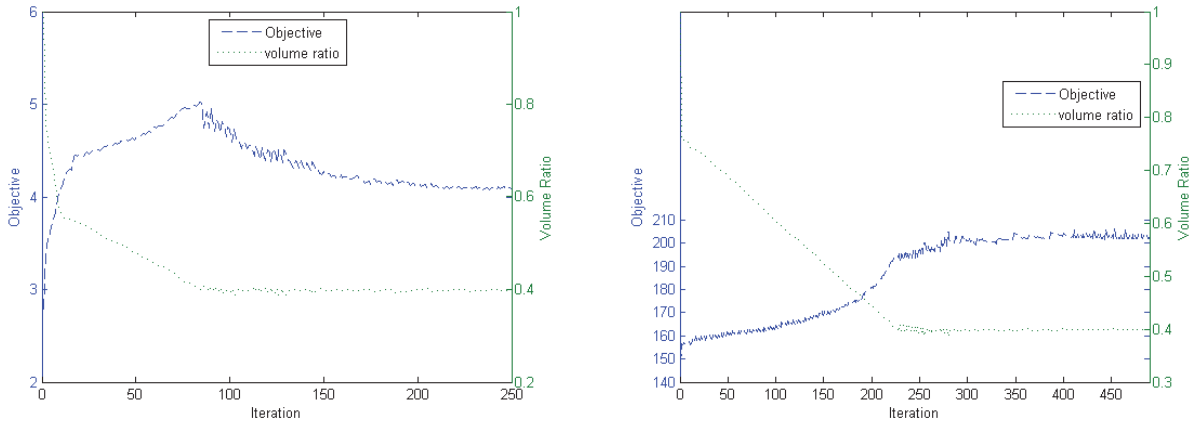

(a) BC1 (b) BC 2

Fig. 15 Convergence histories (the y-axis has the unit of kN·m)

4. Structural skeleton-based path planning

The medial axis transformation-based deposition paths planning was recently proposed by [48,49], which demonstrated outstanding characteristics of producing gap-free cross-section. In fact, the medial axis concept is similar to the structural skeleton concept which was previously studied under the level set

framework for length scale control [46,47]. Therefore, the structural skeleton-based path planning will be adopted in this section to assist the structural topology optimization, and it would be interesting to see if the structural performance can be further enhanced.

4.1 Structural skeleton identification

The first step is to identify the structural skeleton based on the level set information. The procedures previously presented in [47] were utilized, as demonstrate below:

(1) Identify the full skeleton $S(\Omega)$ based on Eq. (23).

$$S(\Omega) = \{(x,y)|\frac{\nabla^2\Phi(x,y)}{\min\left(\nabla^2\Phi(x,y)\right)} \geq \varepsilon_1, \Phi(x,y) > 0\} \tag{23}$$

in which ε_1 is a small positive number to guarantee the numerical computation robustness. Laplacian of the level set function is calculated according to Eq. (24).

$$\nabla^2\Phi(x,y) = \Phi_{i+1,j} + \Phi_{i-1,j} + \Phi_{i,j+1} + \Phi_{i,j-1} - 4\Phi_{i,j} \tag{24}$$

(2) Delete the skeleton points belonging to the corner area $\underline{S}(\Omega)$, i.e.,

$$\bar{S}(\Omega) = S(\Omega)/\underline{S}(\Omega) \tag{25}$$

where,

$$\underline{S}(\Omega) = \{(x,y)|0.5 - 0.5\frac{\nabla^b\Phi(x,y)\cdot\nabla^f\Phi(x,y)}{|\nabla^b\Phi(x,y)|\cdot|\nabla^f\Phi(x,y)|} < \varepsilon_2, \Phi(x,y) < \varepsilon_3\} \tag{26}$$

in which, b and f represent the backward and forward, respectively.

ε_2 is assigned the value 0.6, which works based on the fact that the backward and forward gradients employ opposite signs. ε_3 is a positive number which determines size of the corner area. The purpose of deleting skeleton points among the corner area is to ensure the deposition paths around the skeleton to be continuous.

4.2 Structural skeleton-based path generation

After identification of the skeletons, the points of the skeleton area $\bar{S}(\Omega)$ are assigned the level set value of zero. Then, by solving Eq. (2), the signed distance field is reinitialized and the structural skeleton-based deposition paths are generated. A few examples are demonstrated in Fig. 16, from which we can see that, an interior gap exists in the contour-offset path pattern, but not the structural skeleton-based paths. In addition, a bigger ε_3 will make more paths to be continuous.

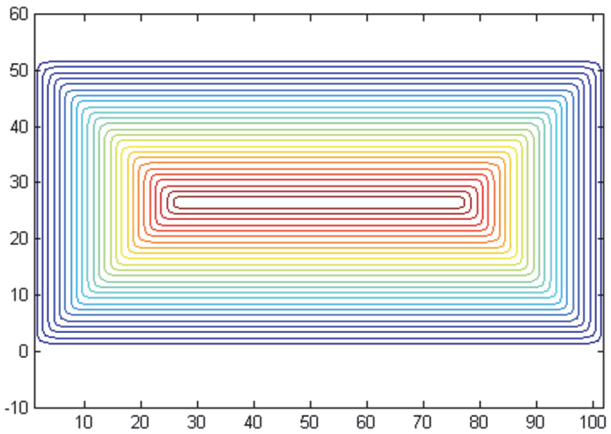

(a) Contour-offset deposition paths

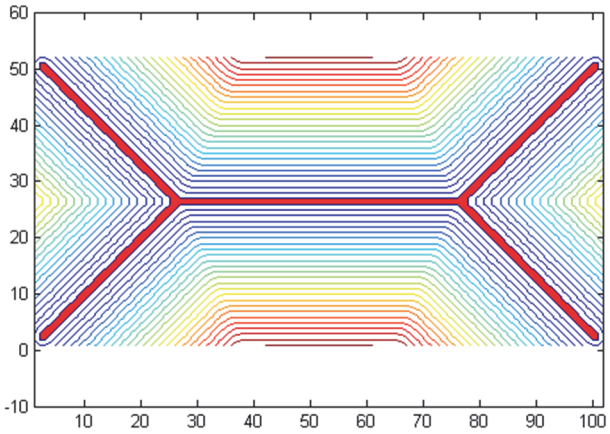

(b) Structural skeleton-based deposition paths ($\varepsilon_3 = 0$)

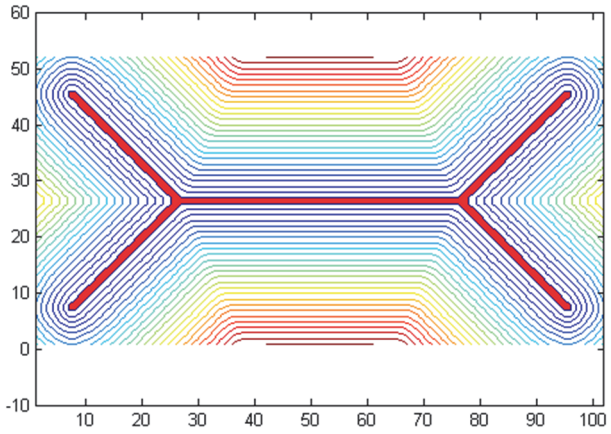

(c) Structural skeleton-based deposition paths ($\varepsilon_3 = 5$)

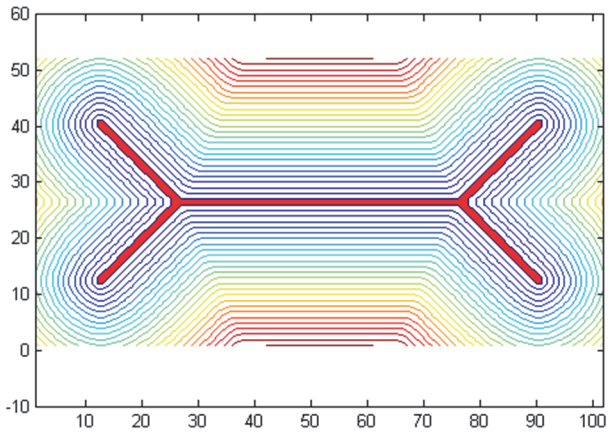

(d) Structural skeleton-based deposition paths ($\varepsilon_3 = 10$)

Fig. 16 Examples of the structural skeleton-based deposition paths ($\varepsilon_1 = 0.2$, $\varepsilon_2 = 0.6$, and the identified skeleton area is filled in red color)

4.3 Deposition path-integrated structural topology optimization

In this sub-section, BC 1 of case 1 and case 2 in Section 3 is re-studied based on the structural skeleton-based deposition path pattern. The optimization results are layer-wisely demonstrated in Fig. 17 and Fig. 18, respectively, where a smaller index means a lower-level layer. In these examples, the parameters of $\varepsilon_1 = 0.1, \varepsilon_2 = 0.6,$ and $\varepsilon_3 = 1.5$ are employed. The numbers in the contour lines represent the signed distance values. The compliances obtained for these two cases are 24.86kN·m and 3.72kN·m.

By comparing with the results in Section 5, the structural skeleton-based deposition paths lead to better structural performance for the BC 1 of case 2, but the improvement of the BC 1 of case 1 is not that obvious. Therefore, it is hard to draw a general conclusion which should be case-specific.

Figure 19 demonstrates the related convergence histories.

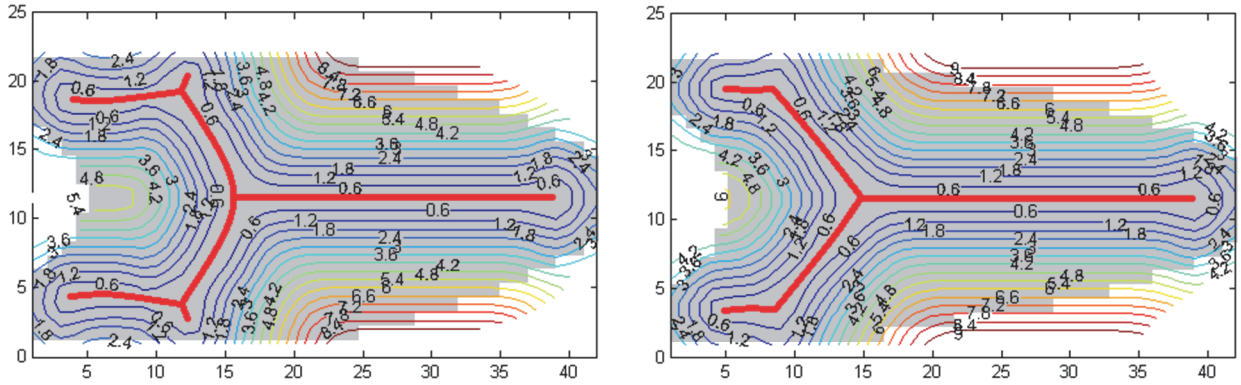

(a) Layer 1 (b) Layer 2

Fig. 17 Layer-wise optimization results of BC1 of case 1 (Compliance = 24.86kN·m)

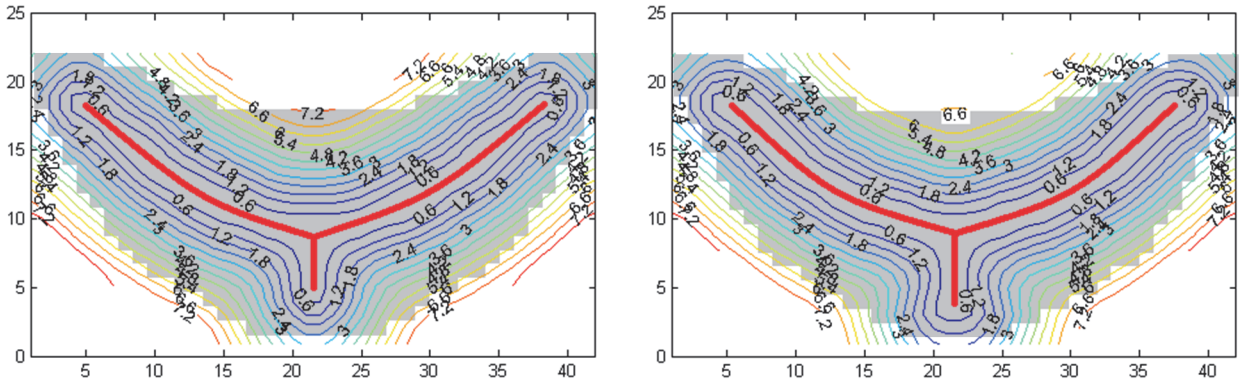

(a) Layer 1 (b) Layer 2

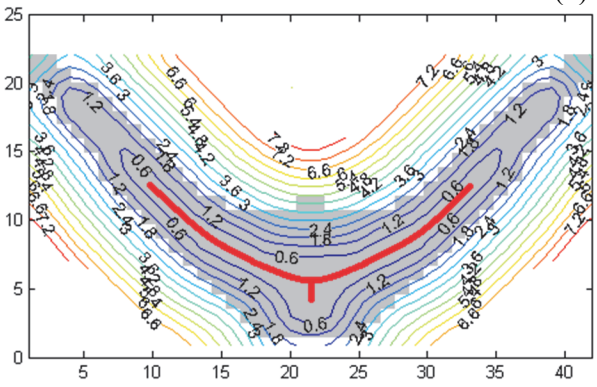

(c) Layer 3

Fig. 18 Layer-wise optimization results of BC1 of case 2 (Compliance = 3.72kN·m)

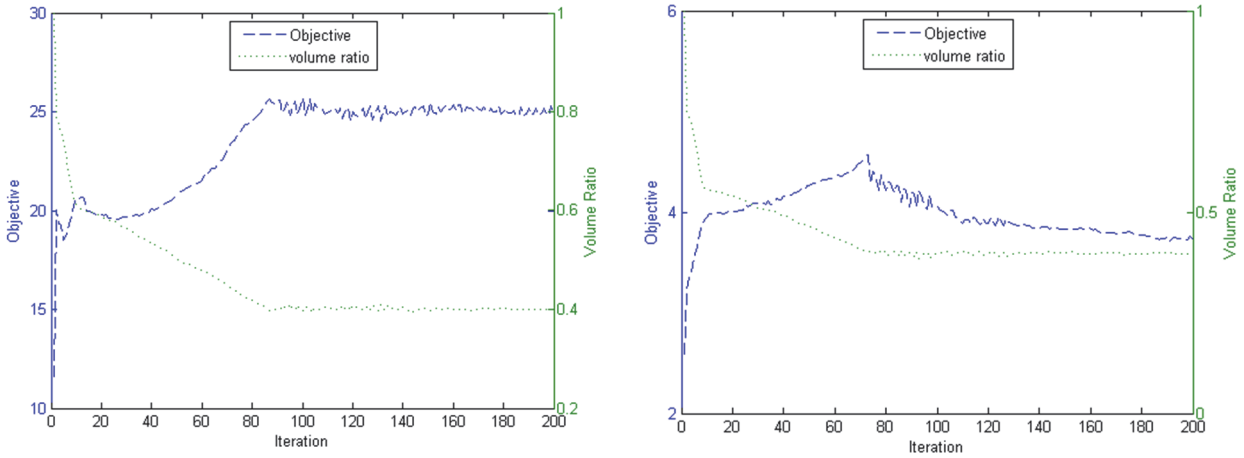

(a) BC1 of case 1 (b) BC1 of case 2

Fig. 19 Convergences histories (the y-axis has the unit of kN·m)

5. Optimization problem type 2: the general 3D self-support design

5.1 Problem formulation and solution

For the more general case where a positive d is involved, solving the related optimization problem is complicated, and the details are presented in this section. For the sake of simplicity, the isotropic material model is assumed where the related deposition paths are not considered.

The multi-level set modeling is realized through Eq. (27).

$$\begin{aligned} \boldsymbol{D}_i &= H(\Phi_i)H(\Phi_{i-1}+d)\boldsymbol{D}, \qquad i>1 \\ \boldsymbol{D}_1 &= H(\Phi_1)\boldsymbol{D} \end{aligned} \tag{27}$$

Then, the compliance minimization problem is re-formulated as shown below:

$$\begin{aligned} \text{min.}\quad J = &\sum_{i=2}^{N}\left[\int_{D_i}\boldsymbol{D}\boldsymbol{e}(\boldsymbol{u}_i)\boldsymbol{e}(\boldsymbol{u}_i)H(\Phi_i)H(\Phi_{i-1}+d)d\Omega_i\right] \\ &+\int_{D_1}\boldsymbol{D}\boldsymbol{e}(\boldsymbol{u}_1)\boldsymbol{e}(\boldsymbol{u}_1)H(\Phi_1)d\Omega_1 \\ s.t.\quad & a(\boldsymbol{u},\boldsymbol{v},\boldsymbol{\Phi}) = l(\boldsymbol{v}), \qquad \forall \boldsymbol{v}\in U_{ad} \\ & V = \sum_{i=1}^{N}\int_{D_i}H(\Phi_i)d\Omega_i \le V_{max} \end{aligned} \tag{28}$$

$$a(\boldsymbol{u},\boldsymbol{v},\boldsymbol{\Phi}) = \sum_{i=2}^{N}\left[\int_{D_i}\boldsymbol{D}\boldsymbol{e}(\boldsymbol{u}_i)\boldsymbol{e}(\boldsymbol{v}_i)H(\Phi_i)H(\Phi_{i-1}+d)d\Omega_i\right]$$

$$+\int_{D_1} \boldsymbol{De}(\boldsymbol{u}_1)\boldsymbol{e}(\boldsymbol{v}_1)H(\Phi_1)d\Omega_1$$

$$l(\boldsymbol{v}) = \int_{\partial\Omega} \boldsymbol{\tau}\cdot\boldsymbol{v}d\Gamma$$

Following a similar process as conducted in Section 3, the adjoint sensitivity analysis is performed on the updated problem and the result is shown below:

$$\begin{aligned} L' = &-\sum_{i=2}^{N}\left[\int_{D_i} \boldsymbol{De}(\boldsymbol{u}_i)\boldsymbol{e}(\boldsymbol{u}_i)\delta(\Phi_i)H(\Phi_{i-1}+d)\Phi_i' d\Omega_i\right] \\ &-\sum_{i=2}^{N}\left[\int_{D_i} \boldsymbol{De}(\boldsymbol{u}_i)\boldsymbol{e}(\boldsymbol{u}_i)H(\Phi_i)\delta(\Phi_{i-1}+d)\Phi_{i-1}' d\Omega_i\right] \\ &-\int_{D_1} \boldsymbol{De}(\boldsymbol{u}_1)\boldsymbol{e}(\boldsymbol{u}_1)\delta(\Phi_1)\Phi_1' d\Omega_1 \\ &+\lambda\sum_{i=1}^{N}\int_{D} \delta(\Phi_i)\Phi_i' d\Omega_i \end{aligned} \tag{29}$$

In Eq. (29), the second term is a contour integral at $\Phi_{i-1} = -d$. However, as well known, only the zero-value level set contour can be effectively updated through solving the Hamilton-Jacobi equation, but not the others. Therefore, it is necessary to transform the second term into an equivalent integral expression but acts on the zero-value level set contour.

To be specific, the following relationship is used to transform the velocity location, referring to [63,64].

$$\int_{\Omega} f(\mathbf{X})d\Omega = \int_{\partial\Omega}\left(\int_{ray_{\partial\Omega}(\mathbf{Y})\cap\Omega} f(\mathbf{Z})[1-dis(\mathbf{Z})\kappa(\mathbf{Y})]d\mathbf{Z}\right)d\Gamma \tag{30}$$

where $\mathbf{X}$ indicates any point located inside the design domain, and $f(\mathbf{X})$ is the integration function; $\mathbf{Y}$ is the boundary point, and $\kappa(\mathbf{Y})$ is the curvature; $\mathbf{Z}$ is the point located on $ray_{\partial\Omega}(\mathbf{Y})$ with the distance $dis(\mathbf{Z})$ from $\mathbf{Y}$. Refer to the following two definitions and Fig. 19 for further details.

Definition 1. For any $\mathbf{X}\in R^n, \Pi_{\partial\Omega}(\mathbf{X}) \coloneqq \{\mathbf{Y}_0\in\partial\Omega, |\mathbf{X}-\mathbf{Y}_0| = inf_{\mathbf{Y}\in\partial\Omega}|\mathbf{X}-\mathbf{Y}|\}$ is the set of projections of $\mathbf{X}$ on $\partial\Omega$. When $\Pi_{\partial\Omega}(\mathbf{X})$ reduces to a single point, it is called the projection $P_{\partial\Omega}(\mathbf{X})$ of $\boldsymbol{X}$ onto $\partial\Omega$.

Definition 2. For any $\mathbf{Y}\in\partial\Omega$, $ray_{\partial\Omega}(\mathbf{Y}) \coloneqq \{\mathbf{Z}\in R^n, dis(\mathbf{Z})\ is\ differentiable\ at\ \mathbf{Z}$ and $P_{\partial\Omega}(\mathbf{Z}) = \mathbf{Y}\}$ is the ray emerging from $\mathbf{Y}$.

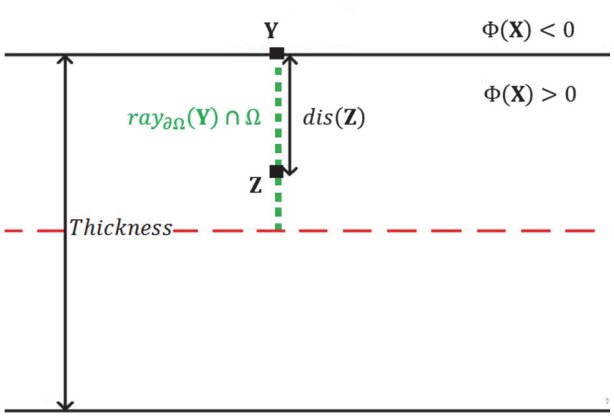

Fig. 20 Schematic plot of the Equation 30 [64]

Based on Eq. (30), the following relationship is derived, as shown in Eq. (31).

$$\int_{D_i} F(\mathbf{X})\delta(\Phi_{i-1})\Phi_{i-1}{}'d\Omega_i = \int_{D_i} F(\mathbf{X})\delta(\Phi_{i-1})\Phi_{i-1}{}'H(\Phi_{i-1}+d)d\Omega_i$$

$$= \int_{D_i}\left[\int_{ray_{\partial\overline{\Omega}}(\mathbf{Y})\cap\overline{\Omega}} F(\mathbf{Z})\delta(\Phi_{i-1})\Phi'_{i-1}(1-(\Phi_{i-1}+d)*k)d\mathbf{Z}\right]\delta(\Phi_{i-1}+d)d\Omega_i \tag{31}$$

$$= \int_{D_i} F(\mathbf{X})\Phi'_{i-1}(1-d*k)\delta(\Phi_{i-1}+d)d\Omega_i$$

where $\overline{\Omega}$ represents the material domain of the level set field $(\Phi_{i-1}+d)$, and $F(\mathbf{X}) = \boldsymbol{De}(\boldsymbol{u}_i)\boldsymbol{e}(\boldsymbol{u}_i)H(\Phi_i)$ at $P_{\partial\overline{\Omega}}(\mathbf{X})$. Therefore, the second term in Eq. (29) can be transformed into:

$$-\sum_{i=2}^{N}\left[\int_{D_i} F(\mathbf{X})\delta(\Phi_{i-1}+d)\Phi_{i-1}{}'d\Omega_i\right]$$

$$= -\sum_{i=2}^{N}\left[\int_{D_i}\frac{F(\mathbf{X})}{(1-d*k)}\delta(\Phi_{i-1})\Phi_{i-1}{}'d\Omega_i\right] \tag{32}$$

In summary, the sensitivity result is adapted into:

$$L' = -\sum_{i=2}^{N}\left[\int_{D_i}\boldsymbol{De}(\boldsymbol{u}_i)\boldsymbol{e}(\boldsymbol{u}_i)\delta(\Phi_i)H(\Phi_{i-1}+d)\Phi_i{}'d\Omega_i\right]$$

$$-\sum_{i=2}^{N}\left[\int_{D_i}\frac{F(\mathbf{X})}{(1-d*k)}\delta(\Phi_{i-1})\Phi_{i-1}{}'d\Omega_i\right] \tag{33}$$

$$-\int_{D_1} \boldsymbol{De}(\boldsymbol{u}_1)\boldsymbol{e}(\boldsymbol{u}_1)\delta(\Phi_1)\Phi_1' d\Omega_1$$

$$+\lambda \sum_{i=1}^{N} \int_{D} \delta(\Phi_i)\Phi_i' d\Omega_i$$

Now, the sensitivity result is completely composed of integrals on the zero-value level set contours. The boundary velocity fields can be trivially derived based on the principle of decreasing the Lagrangian, and thus the level set fields can be updated through solving the Hamilton Jacobi equation. The design update method is well-established and interested readers can refer to [33,34,65] for the details.

5.2 Numerical examples

Two numerical examples are studied to demonstrate the effectiveness of the self-support design with the positive d value.

Figure 21 presents the input design domain (L40cm*W20cm*H30cm) and the attached boundary conditions. A set of forces are loaded at the left bottom edge of the magnitude 5kN/cm, and the right side face is fixed. The solid material employs a Young's modulus value of 1GPa and Poisson ratio value of 0.3. The optimization problem is to minimize the structural compliance under the maximum material volume fraction of 0.5.

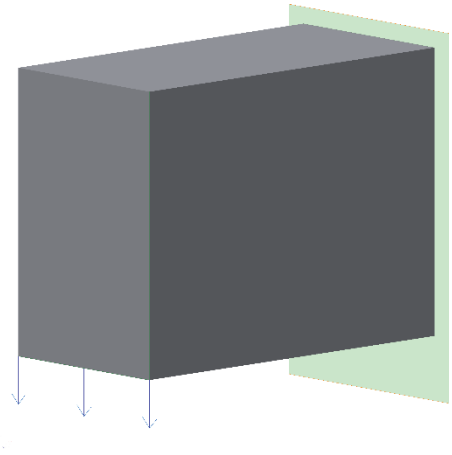

Fig. 21 The cantilever problem

Correspondingly, the optimization results with and without considering the self-support requirement are demonstrated in Fig. 22 and Fig. 23, respectively. For the former, the maximally-allowable overhang distance $d = 1$ is assumed, which also means the threshold inclination angle of 45 degree. It can be clearly observed from the results that, the smallest inclination angle in Fig. 22 is constrained above 45 degree, while that in Fig. 23 is much smaller than 45 degree.

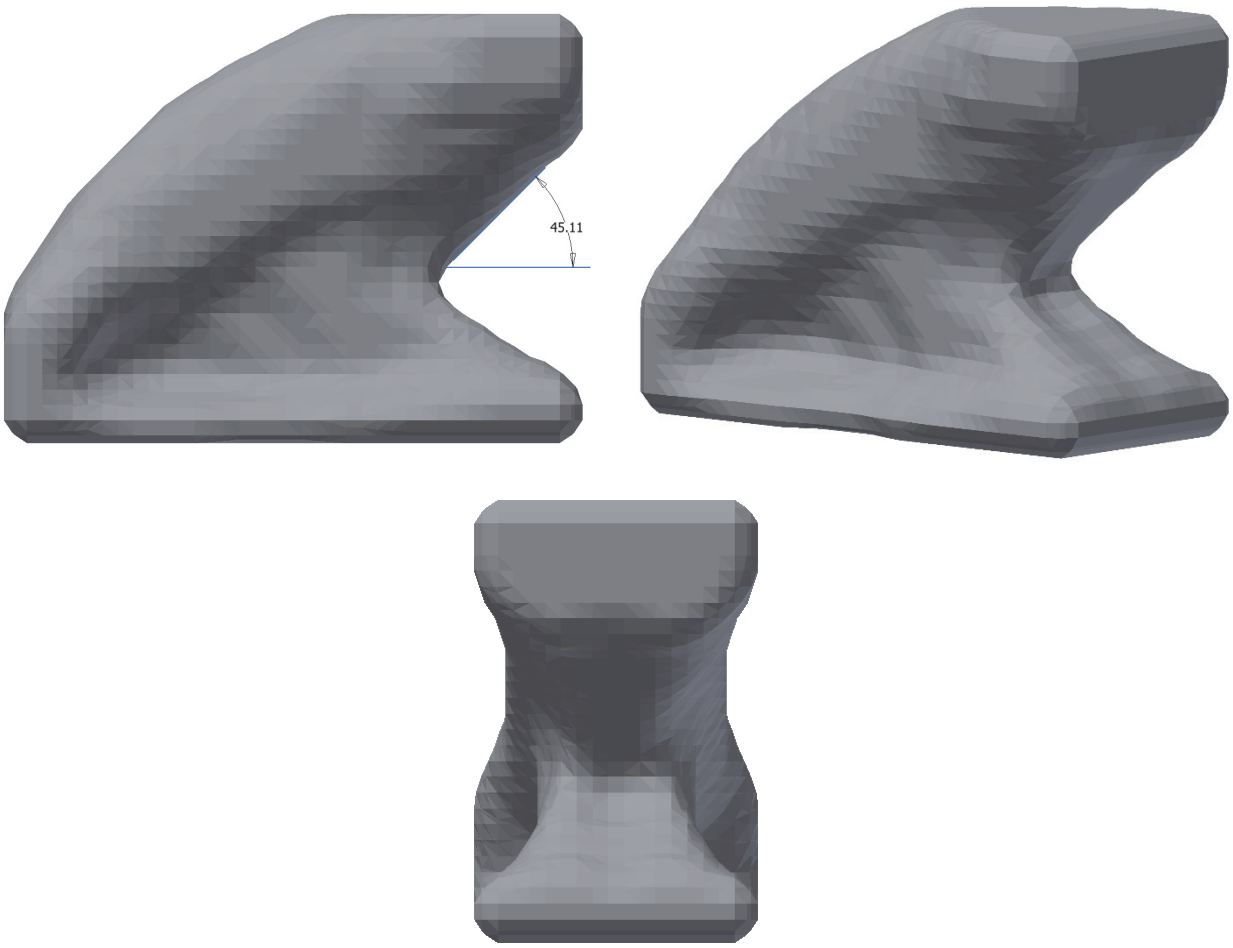

Fig. 22 The optimization result with considering the self-support requirement (measured minimum inclination angle of 45.11 degree and the structural compliance of 1.64kN·m)

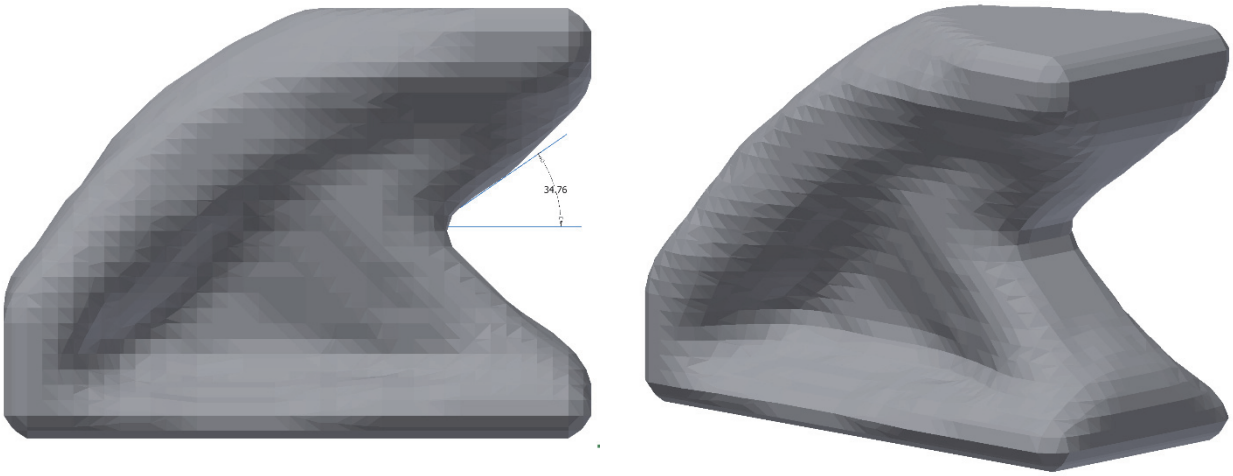

Fig. 23 The optimization result without considering the self-support requirement (measured minimum inclination angle of 34.76 degree and the structural compliance of 1.59kN·m)

Figure 24 presents the input design domain (L80cm*W20cm*H15cm) and the attached boundary conditions. A set of forces are loaded at the top center of magnitude 5kN/cm, and the two bottom edges are fixed. The solid material employs a Young's modulus value of 1GPa and Poisson ratio value of 0.3 by assumption. The optimization problem is to minimize the structural compliance under the maximum material volume faction of 0.5.

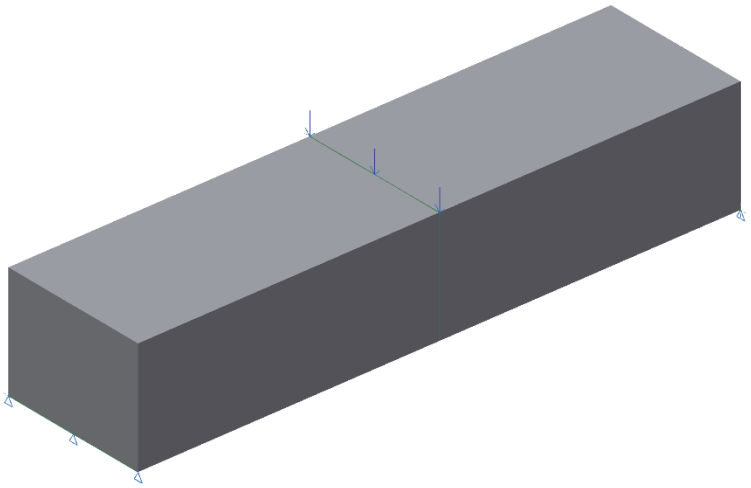

Fig. 24 The double-clamped beam problem

Correspondingly, the optimization results with and without considering the self-support requirement are demonstrated in Fig. 25 and Fig. 27, respectively. For the former, the maximally-allowable overhang distance $d = 1$ is assumed, and in Fig. 26, the major overhang areas have been measured from different view angles. It is concluded that the inclination angles have been constrained above 45 degree, while some minor violations exist because of the post-treatment process (smoothing) into a STL model. On the other hand, without considering the self-support requirement, the overhang areas with the inclination angle below 45 degree are marked out in Fig. 28. Therefore, effectiveness of the proposed method is proved. It is noted that, only the left half of the structure is demonstrated because of symmetry.

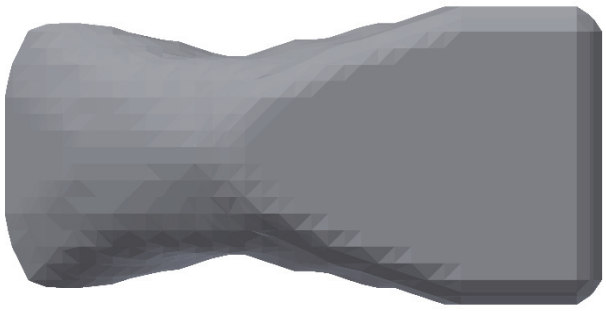

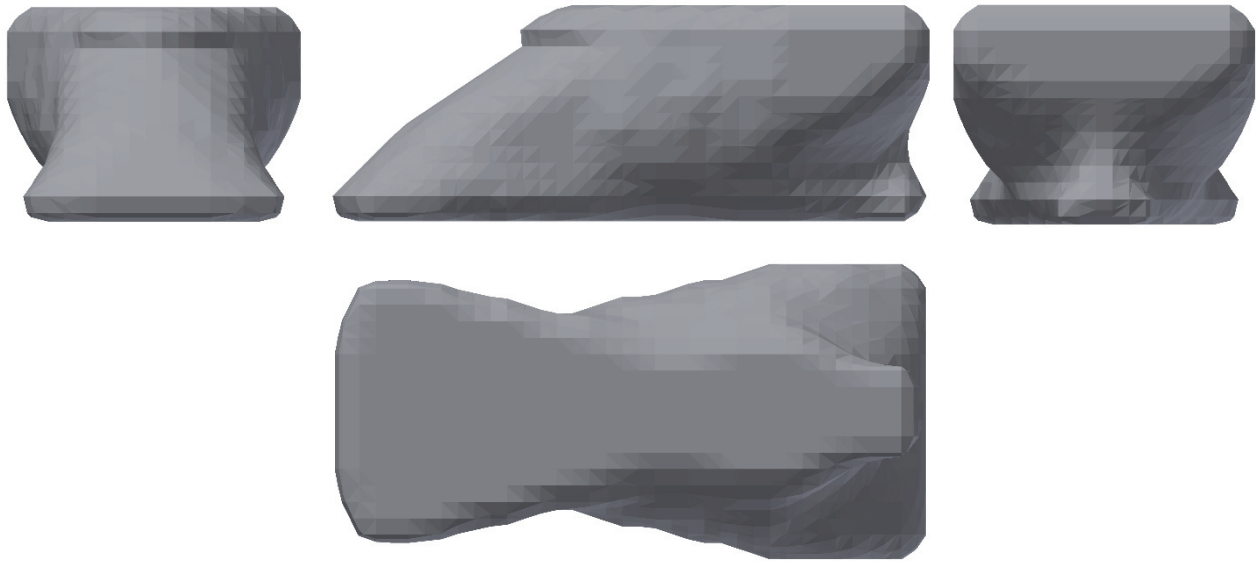

Fig. 25 The optimization result with considering the self-support requirement (the structural compliance of 3.39kN·m)

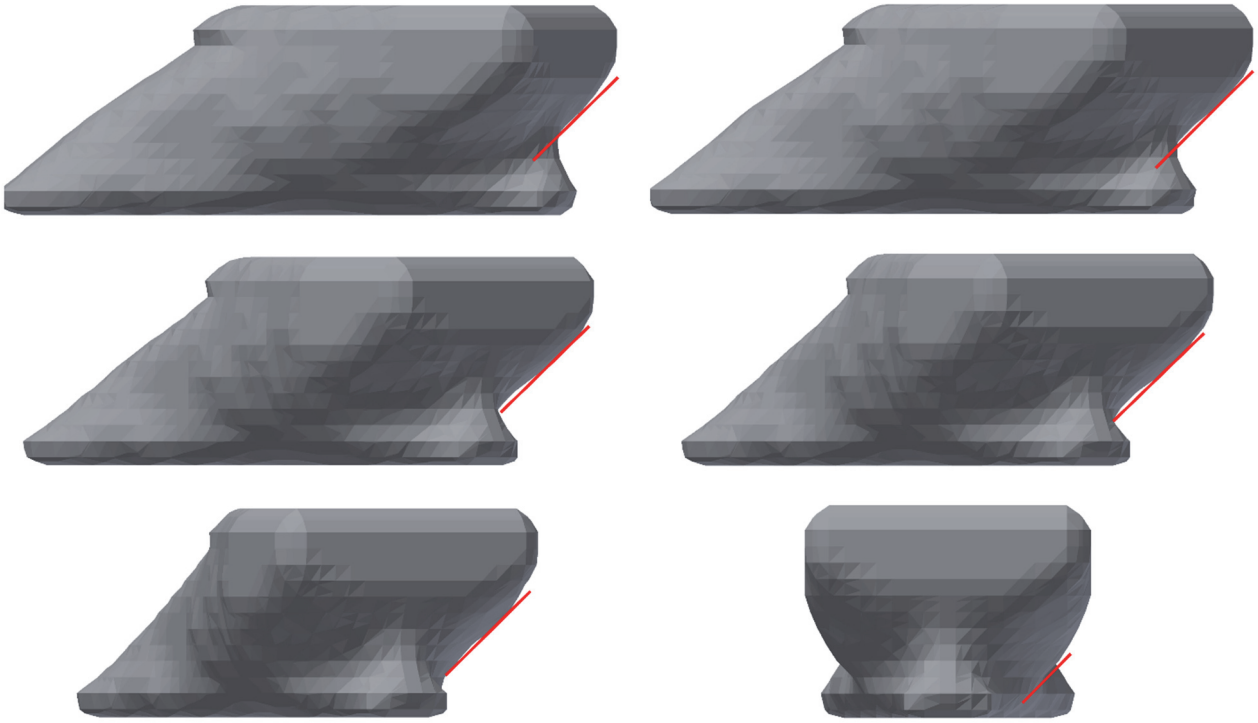

Fig. 26 Measurement of the overhang inclination angles (The red line indicates the angle of 45 degree)

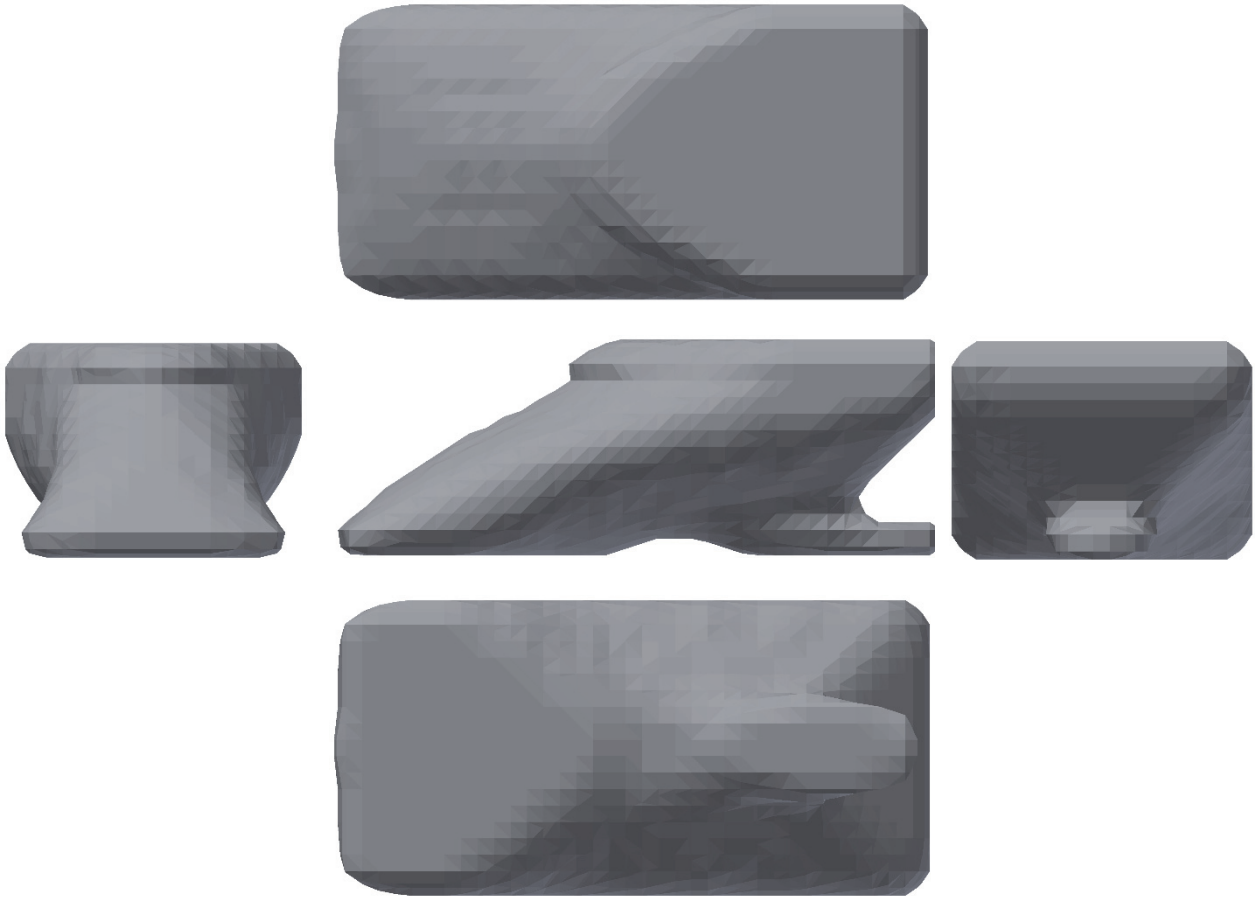

Fig. 27 The optimization result with considering the self-support requirement (the structural compliance of 3.19kN·m)

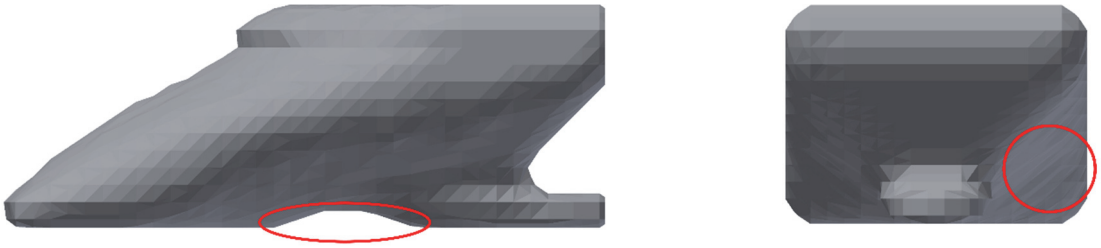

Fig. 28 Overhang areas with the inclination angle below 45 degree (marked out by the red circles)

The convergence histories of the cantilever and beam examples are shown in Fig. 29.

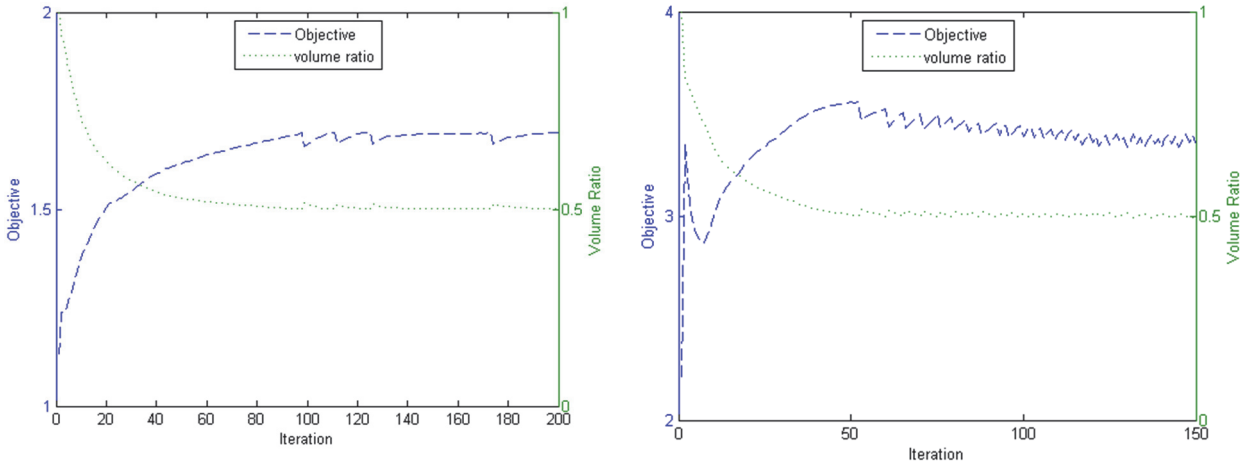

(a) cantilever example (b) beam example

Fig. 29 Convergence histories

5.3. A combined case study

It is straight-forward to extend the general support-free problem formulation in Eq. (28) to consider the deposition path-induced material anisotropy, and a related problem is studied in this sub-section.

As shown in Fig. 30, the top surface of the cube is imposed of uniform pressure forces with the magnitude of 1kN/cm^2 and the four bottom corners are fixed. The cube size is 30cm*30cm*20cm, and its boundary frame is non-designable, which therefore, belongs to a problem of self-support enclosed void design. The optimization problem is still compliance minimization and 15 percent of materials will be removed. The material properties as shown in Table 1 is used. The part is sliced into 15 layers and the threshold self-support inclination angle is 45 degree.

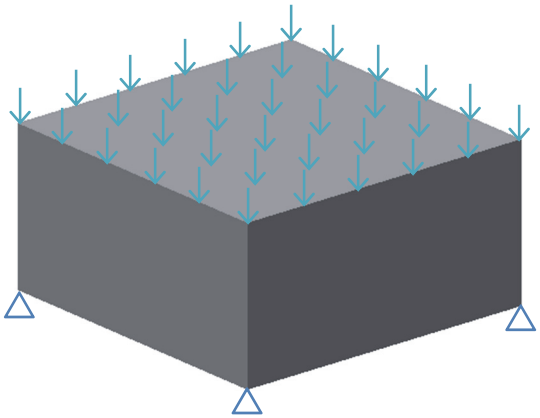

Fig. 30 Boundary conditions of the cube problem

The optimization result is demonstrated in Fig. 31 and the deposition paths at selected layers are shown in Fig. 32, where the void area in each layer is filled in grey color. It can be observed from Fig. 31 that, the enclosed void forms the shape of a pyramid and one of the inclined surface is measured about the

inclination angle. Referring to the 45 degree reference line (in red color), the inclined surface can be self-support and because of being symmetric, the whole enclosed void can be self-support.

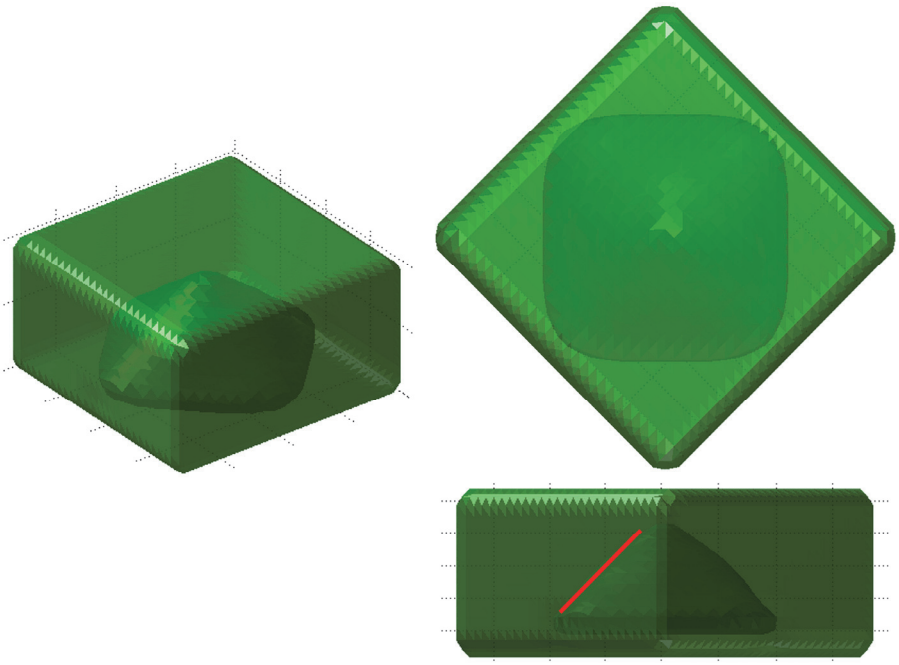

Fig. 31 Self-support enclosed void design (the structural compliance of 11.79 kN·m)

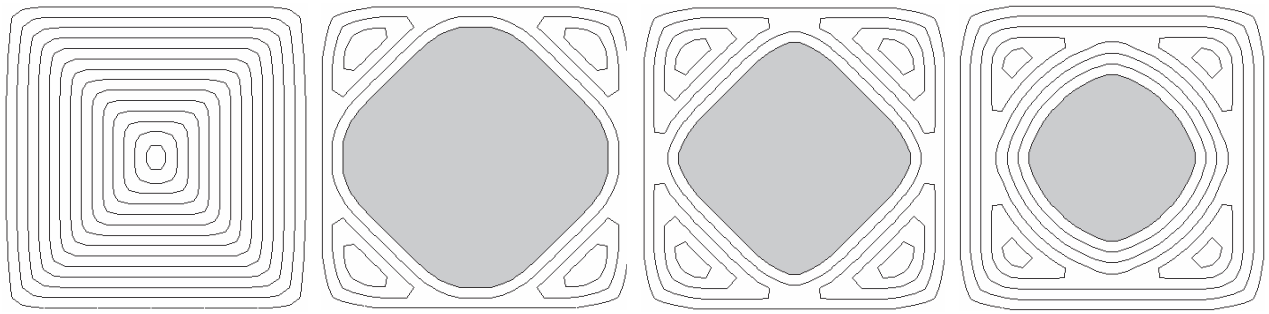

(a) Layer 1 (b) Layer 3 (c) Layer 5 (d) Layer 7

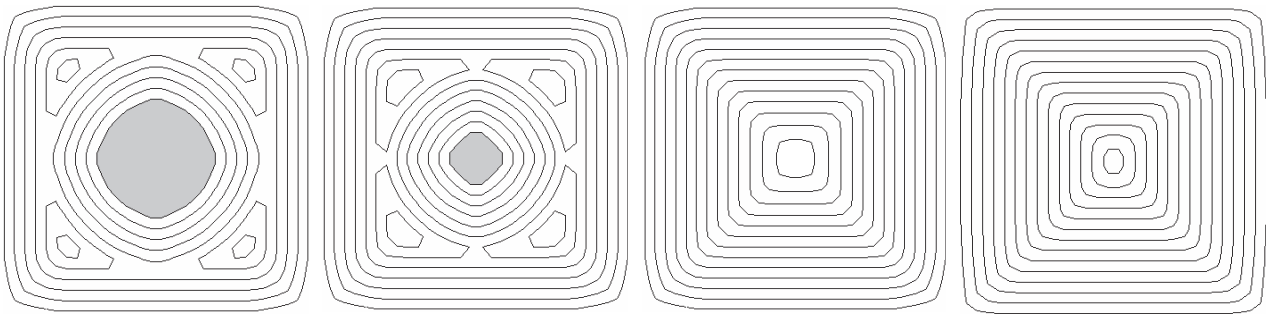

(e) Layer 9 (f) Layer 11 (g) Layer 13 (h) Layer 15

Fig. 32 Contour-offset deposition paths at selected layers

6. Conclusion

In this paper, deposition path planning is concurrently performed when doing topology optimization, and thus, the AM-induced anisotropic material properties are well addressed for realistic structural performance evaluation. Two deposition path patterns are studied, e.g. the contour-offset and the structural skeleton-based.

Moreover, the support-free manufacturability constraint is tackled. Multiple level set functions are used to represent the sliced AM part and a novel multi-level set interpolation has been proposed to address the support-free manufacturability constraint. It is proven by several numerical examples that effective overhang-free design can be generated. It is noted that, the proposed approach shows the advantage that the sensitivity analysis is computationally efficient, where it consumes less than 2 percent of the time taken by the FEA. Specifically, the sensitivity analysis takes 0.77, 0.38, 0.44 seconds on average and the FEA takes 117.39, 29.53, 103.59 seconds for the cantilever, beam, and cube problems, respectively, where the sensitivity costs are only 0.66%, 1.28%, and 0.42% of the FEA costs. Noted that, the program is run in Matlab 2011a with Intel Xeon CPU E5-1600 at 3.00GHz.

For future work, there is still room to further modify the structure skeleton-based deposition path planning algorithm, through which the structural performance can be more accurately evaluated. The numerical stability and computational efficiency of the 3D problems will also be focused.

Acknowledgement

The authors would like to acknowledge the support from China Scholarship Council (CSC) and the National Science Foundation (CMMI-1634261).

Reference

[1] Rosen DW. Computer-Aided Design for Additive Manufacturing of Cellular Structures. Comput-Aided Des Appl 2007;4:585–94. doi:10.1080/16864360.2007.10738493.

[2] Ponche R, Kerbrat O, Mognol P, Hascoet J-Y. A novel methodology of design for Additive Manufacturing applied to Additive Laser Manufacturing process. Robot Comput-Integr Manuf 2014;30:389–98. doi:10.1016/j.rcim.2013.12.001.

[3] Ponche R, Hascoet JY, Kerbrat O, Mognol P. A new global approach to design for additive manufacturing. Virtual Phys Prototyp 2012;7:93–105. doi:10.1080/17452759.2012.679499.

[4] Yang S, Zhao YF. Additive manufacturing-enabled design theory and methodology: a critical review. Int J Adv Manuf Technol 2015;80:327–42. doi:10.1007/s00170-015-6994-5.

[5] Liu J. Guidelines for AM part consolidation. Virtual Phys Prototyp 2016;11:133–41. doi:10.1080/17452759.2016.1175154.

[6] Gao W, Zhang Y, Ramanujan D, Ramani K, Chen Y, Williams CB, et al. The status, challenges, and future of additive manufacturing in engineering. Comput-Aided Des 2015;69:65–89. doi:10.1016/j.cad.2015.04.001.

[7] Zhang P, Toman J, Yu Y, Biyikli E, Kirca M, Chmielus M, et al. Efficient Design-Optimization of Variable-Density Hexagonal Cellular Structure by Additive Manufacturing: Theory and Validation. J Manuf Sci Eng 2015;137:021004–021004. doi:10.1115/1.4028724.
[8] Tang Y, Kurtz A, Zhao YF. Bidirectional Evolutionary Structural Optimization (BESO) based design method for lattice structure to be fabricated by additive manufacturing. Comput-Aided Des 2015;69:91–101. doi:10.1016/j.cad.2015.06.001.
[9] Cheng L, Zhang P, Biyikli E, Bai J, Robbins J, Lynch ME, et al. Efficient Design Optimization of Variable-Density Cellular Structures for Additive Manufacturing: Theory and Experimental Validation. Rapid Prototyp J 2016.
[10] Gaynor AT, Meisel NA, Williams CB, Guest JK. Multiple-Material Topology Optimization of Compliant Mechanisms Created Via PolyJet Three-Dimensional Printing. J Manuf Sci Eng 2014;136:061015. doi:10.1115/1.4028439.
[11] Maute K, Tkachuk A, Wu J, Jerry Qi H, Ding Z, Dunn ML. Level Set Topology Optimization of Printed Active Composites. J Mech Des 2015;137:111402. doi:10.1115/1.4030994.
[12] Leary M, Merli L, Torti F, Mazur M, Brandt M. Optimal topology for additive manufacture: A method for enabling additive manufacture of support-free optimal structures. Mater Des 2014;63:678–90. doi:10.1016/j.matdes.2014.06.015.
[13] Gaynor AT, Guest JK. Topology optimization considering overhang constraints: Eliminating sacrificial support material in additive manufacturing through design. Struct Multidiscip Optim 2016:1–16. doi:10.1007/s00158-016-1551-x.
[14] Langelaar M. An additive manufacturing filter for topology optimization of print-ready designs. Struct Multidiscip Optim 2016:1–13. doi:10.1007/s00158-016-1522-2.
[15] Brackett D, Ashcroft I, Hague R. TOPOLOGY OPTIMIZATION FOR ADDITIVE MANUFACTURING, Austin, TX: 2011.
[16] Gardan N, Schneider A. Topological optimization of internal patterns and support in additive manufacturing. J Manuf Syst 2015;37, Part 1:417–25. doi:10.1016/j.jmsy.2014.07.003.
[17] Zegard T, Paulino GH. Bridging topology optimization and additive manufacturing. Struct Multidiscip Optim 2015;53:175–92. doi:10.1007/s00158-015-1274-4.
[18] Vogiatzis P, Chen S, Zhou C. An Open Source Framework For Integrated Additive Manufacturing And Level-Set Based Topology Optimization. ASME J Comput Inf Sci Eng 2017.
[19] Meisel N, Williams C. An Investigation of Key Design for Additive Manufacturing Constraints in Multimaterial Three-Dimensional Printing. J Mech Des 2015;137:111406. doi:10.1115/1.4030991.
[20] Liu J, Ma Y. A survey of manufacturing oriented topology optimization methods. Adv Eng Softw 2016;100:161–75. doi:10.1016/j.advengsoft.2016.07.017.
[21] Ahn SH, Montero M, Odell D, Roundy S, Wright PK. Anisotropic material properties of fused deposition modeling ABS. Rapid Prototyp J 2002;8:248–57. doi:10.1108/13552540210441166.
[22] Bellini A, Güçeri S. Mechanical characterization of parts fabricated using fused deposition modeling. Rapid Prototyp J 2003;9:252–64. doi:10.1108/13552540310489631.
[23] Huang B, Singamneni S. Raster angle mechanics in fused deposition modelling. J Compos Mater 2014:0021998313519153. doi:10.1177/0021998313519153.
[24] Hill N, Haghi M. Deposition direction-dependent failure criteria for fused deposition modeling polycarbonate. Rapid Prototyp J 2014;20:221–7. doi:10.1108/RPJ-04-2013-0039.
[25] Zhang P, Liu J, To AC. Role of anisotropic properties on topology optimization of additive manufactured load bearing structures. Scr Mater 2016. doi:http://dx.doi.org/10.1016/j.scriptamat.2016.10.021.
[26] Zhou Q, Panetta J, Zorin D. Worst-case Structural Analysis. ACM Trans Graph 2013;32:137:1–137:12. doi:10.1145/2461912.2461967.
[27] Ulu E, Korkmaz E, Yay K, Ozdoganlar OB, Kara LB. Enhancing the Structural Performance of Additively Manufactured Objects Through Build Orientation Optimization. J Mech Des 2015;137:111410. doi:10.1115/1.4030998.

[28] Zhang P, To AC. Transversely isotropic hyperelastic-viscoplastic model for glassy polymers with application to additive manufactured photopolymers. Int J Plast 2016;80:56–74. doi:10.1016/j.ijplas.2015.12.012.
[29] Umetani N, Schmidt R. Cross-sectional Structural Analysis for 3D Printing Optimization. SIGGRAPH Asia 2013 Tech. Briefs, New York, NY, USA: ACM; 2013, p. 5:1–5:4. doi:10.1145/2542355.2542361.
[30] Smith DE, Hoglund R. CONTINUOUS FIBER ANGLE TOPOLOGY OPTIMIZATION FOR POLYMER FUSED FILLAMENT FABRICATION. 2016 Annu. Int. Solid Free. Fabr. Symp., Austin, TX: 2016.
[31] Liu J, Yu H. Concurrent deposition path planning and structural topology optimization for additive manufacturing. Rapid Prototyp J 2017;23.
[32] Osher S, Sethian JA. Fronts propagating with curvature-dependent speed: Algorithms based on Hamilton-Jacobi formulations. J Comput Phys 1988;79:12–49. doi:10.1016/0021-9991(88)90002-2.
[33] Wang MY, Wang X, Guo D. A level set method for structural topology optimization. Comput Methods Appl Mech Eng 2003;192:227–46. doi:10.1016/S0045-7825(02)00559-5.
[34] Allaire G, Jouve F, Toader A-M. Structural optimization using sensitivity analysis and a level-set method. J Comput Phys 2004;194:363–93. doi:10.1016/j.jcp.2003.09.032.
[35] Wang S, Wang MY. Radial basis functions and level set method for structural topology optimization. Int J Numer Methods Eng 2006;65:2060–90. doi:10.1002/nme.1536.
[36] Chen J, Shapiro V, Suresh K, Tsukanov I. Shape optimization with topological changes and parametric control. Int J Numer Methods Eng 2007;71:313–46. doi:10.1002/nme.1943.
[37] Liu J, Ma Y-S. 3D level-set topology optimization: a machining feature-based approach. Struct Multidiscip Optim 2015;52:563–82. doi:10.1007/s00158-015-1263-7.
[38] van Dijk NP, Maute K, Langelaar M, van Keulen F. Level-set methods for structural topology optimization: a review. Struct Multidiscip Optim 2013;48:437–72. doi:10.1007/s00158-013-0912-y.
[39] Zhou S, Li Q. A variational level set method for the topology optimization of steady-state Navier–Stokes flow. J Comput Phys 2008;227:10178–95. doi:10.1016/j.jcp.2008.08.022.
[40] Zhuang C, Xiong Z, Ding H. A level set method for topology optimization of heat conduction problem under multiple load cases. Comput Methods Appl Mech Eng 2007;196:1074–84. doi:10.1016/j.cma.2006.08.005.
[41] Yamada T, Izui K, Nishiwaki S. A Level Set-Based Topology Optimization Method for Maximizing Thermal Diffusivity in Problems Including Design-Dependent Effects. J Mech Des 2011;133:031011–031011. doi:10.1115/1.4003684.
[42] Shen H, Fu J, Chen Z, Fan Y. Generation of offset surface for tool path in NC machining through level set methods. Int J Adv Manuf Technol 2010;46:1043–7. doi:10.1007/s00170-009-2164-y.
[43] Zhuang C, Xiong Z, Ding H. High speed machining tool path generation for pockets using level sets. Int J Prod Res 2010;48:5749–66. doi:10.1080/00207540903232771.
[44] Blum H. A Transformation for Extracting New Descriptors of Shape. Models Percept. Speech Vis. Form, MIT press; 1967, p. 362–80.
[45] Zhang W, Zhong W, Guo X. An explicit length scale control approach in SIMP-based topology optimization. Comput Methods Appl Mech Eng 2014;282:71–86. doi:10.1016/j.cma.2014.08.027.
[46] Guo X, Zhang W, Zhong W. Explicit feature control in structural topology optimization via level set method. Comput Methods Appl Mech Eng 2014;272:354–78. doi:10.1016/j.cma.2014.01.010.
[47] Xia Q, Shi T. Constraints of distance from boundary to skeleton: For the control of length scale in level set based structural topology optimization. Comput Methods Appl Mech Eng 2015;295:525–42. doi:10.1016/j.cma.2015.07.015.
[48] Ding D, Pan Z, Cuiuri D, Li H. A practical path planning methodology for wire and arc additive manufacturing of thin-walled structures. Robot Comput-Integr Manuf 2015;34:8–19. doi:10.1016/j.rcim.2015.01.003.

[49] Ding D, Pan Z, Cuiuri D, Li H, van Duin S, Larkin N. Bead modelling and implementation of adaptive MAT path in wire and arc additive manufacturing. Robot Comput-Integr Manuf 2016;39:32–42. doi:10.1016/j.rcim.2015.12.004.
[50] Hu K, Jin S, Wang CCL. Support slimming for single material based additive manufacturing. Comput-Aided Des 2015;65:1–10. doi:10.1016/j.cad.2015.03.001.
[51] Mirzendehdel AM, Suresh K. Support structure constrained topology optimization for additive manufacturing. Comput-Aided Des 2016;81:1–13. doi:10.1016/j.cad.2016.08.006.
[52] Gaynor AT. Topology Optimization Algorithms for Additive Manufacturing. 2015.
[53] Langelaar M. Topology optimization of 3D self-supporting structures for additive manufacturing. Addit Manuf 2016;12, Part A:60–70. doi:10.1016/j.addma.2016.06.010.
[54] Qian X. Undercut and Overhang Angle Control in Topology Optimization: a Density Gradient based Integral Approach. Int J Numer Methods Eng n.d.:n/a-n/a. doi:10.1002/nme.5461.
[55] Wu J, Wang CCL, Zhang X, Westermann R. Self-supporting rhombic infill structures for additive manufacturing. Comput-Aided Des 2016;80:32–42. doi:10.1016/j.cad.2016.07.006.
[56] Brampton CJ, Wu KC, Kim HA. New optimization method for steered fiber composites using the level set method. Struct Multidiscip Optim 2015;52:493–505. doi:10.1007/s00158-015-1256-6.
[57] Wang MY, Wang X. "Color" level sets: a multi-phase method for structural topology optimization with multiple materials. Comput Methods Appl Mech Eng 2004;193:469–96. doi:10.1016/j.cma.2003.10.008.
[58] Wang MY, Chen S, Wang X, Mei Y. Design of Multimaterial Compliant Mechanisms Using Level-Set Methods. J Mech Des 2005;127:941–56. doi:10.1115/1.1909206.
[59] Wang MY, Wang X. A level-set based variational method for design and optimization of heterogeneous objects. Comput-Aided Des 2005;37:321–37. doi:10.1016/j.cad.2004.03.007.
[60] Guo X, Zhang W, Zhong W. Stress-related topology optimization of continuum structures involving multi-phase materials. Comput Methods Appl Mech Eng 2014;268:632–55. doi:10.1016/j.cma.2013.10.003.
[61] Wang Y, Luo Z, Kang Z, Zhang N. A multi-material level set-based topology and shape optimization method. Comput Methods Appl Mech Eng 2015;283:1570–86. doi:10.1016/j.cma.2014.11.002.
[62] Liu J, Ma Y. Sustainable Design-Oriented Level Set Topology Optimization. J Mech Des 2017;139:011403 (1-8). doi:10.1115/1.4035052.
[63] Allaire G, Dapogny C, Delgado G, Michailidis G. Multi-phase structural optimization via a level set method. ESAIM Control Optim Calc Var 2014;20:576–611.
[64] Liu J, Ma Y, Fu J, Duke K. A novel CACD/CAD/CAE integrated design framework for fiber-reinforced plastic parts. Adv Eng Softw 2015;87:13–29. doi:10.1016/j.advengsoft.2015.04.013.
[65] Osher S, Fedkiw R. Level Set Methods and Dynamic Implicit Surfaces. vol. 153. New York, NY: Springer New York; 2003.